Sotoudeh Heidarpour

Residual Stress in Stellite 6 Layers Deposited on Austenitic Stainless Steel Substrate using GMAW-WAAM

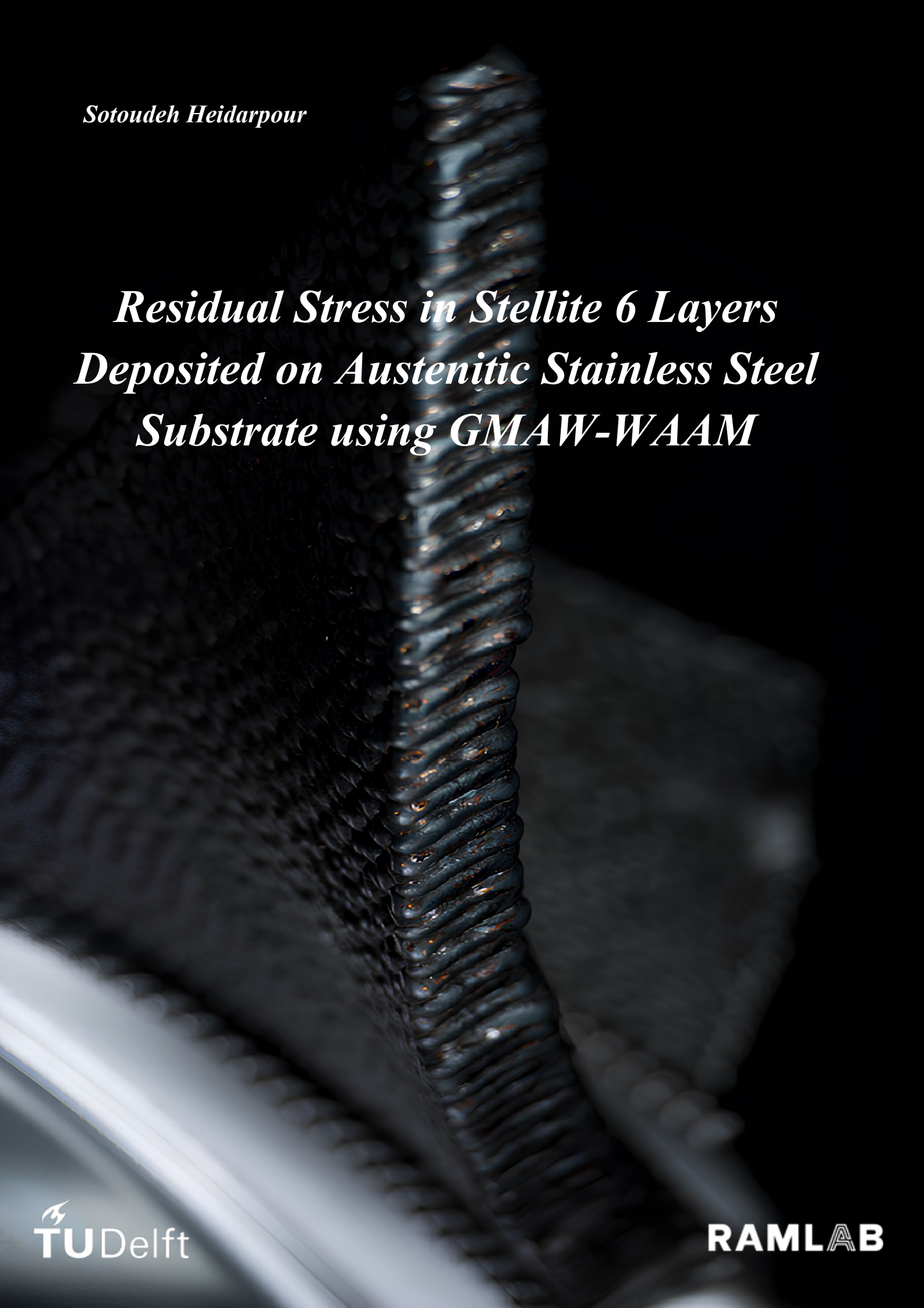

TU Delft

RAMLAB

Residual Stress in Stellite 6 Layers Deposited on Austenitic Stainless Steel Substrate using GMAW-WAAM

By

Sotoudeh Heidarpour

in partial fulfilment of the requirements for the degree of

Master of Science
in Materials Science and Engineering

at the Delft University of Technology,
to be defended publicly on Thursday October 31, 2024 at 10:00 AM.

Supervisor:	Dr. ir. M.J.M Hermans, TU Delft
	Dr. ir. Wei Ya, RAMLAB BV
Thesis committee:	Dr.ir. I. Apachitei, TU Delft

Acknowledgements

As I reach the culmination of my master's program at Delft University of Technology, I am filled with immense gratitude for those who have supported me on this journey.

First and foremost, I must express my heartfelt thanks to my parents, whose support has been the foundation of my scientific journey. Their belief in me gave me the wings to pursue my dreams and reach this point in my Master's program at TU Delft.

I am deeply grateful to Vincent Wegener for the chance to work at RAMLAB on this project. A special thanks goes to my company supervisor, Dr. Wei Ya, whose expert guidance and knowledge in additive manufacturing have been crucial in shaping my research and pushing me to improve. My appreciation extends to Aditya, Jakub, Remco, and everyone at RAMLAB for their invaluable support. Additionally, I want to thank my university supervisor, Dr. Marcel Hermans, for introducing me to RAMLAB and providing me with insightful guidance throughout this fascinating research.

I am thankful to the mechanical engineering faculty at TU Delft for creating a supportive environment that has allowed me to grow both personally and academically. The experiences I have had as a graduate student here will stay with me forever. I also want to express my gratitude to my friends for their support throughout my master's program.

Lastly, I owe an immeasurable debt of gratitude to my family, and especially to my husband, for their unconditional and emotional support throughout my graduate studies. Their patience and understanding through the lengthy process of completing this thesis have been a source of great comfort and motivation.

Thank you all from the bottom of my heart.

Sotoudeh Heidarpour
Delft, October 2024

Dedication

To my husband, Arshia Ghasemidolatsara,
my father, Amir Heidarpour,
my mother, Arezoo Heidarpour,
and my sister, Saba Heidarpour.

Abstract

This thesis describes an investigation of the deposition of Stellite 6 on SS316L stainless steel substrates using a Gas Metal Arc Welding (GMAW) based Wire Arc Additive Manufacturing (WAAM) system. The primary aim of this research was to optimize the deposition process with a focus on reducing heat input and understanding the development of residual stress, a critical factor in the performance of hardfacing materials. The project utilized a zigzag toolpath deposition strategy requested by adaptation from current manual operation, aiming to achieve low heat input while maintaining layer integrity.

The experimental methods involved finite element analysis (FEA) to simulate the deformation of the sample for a better understanding of the material thermo-mechanical responses to the zigzag deposition strategy used. The deformation simulation agrees with the measured deflection. The model, however, computed very large residual stresses. To have a better evaluation of the residual stress resulted from the deposition process, Incremental Central Hole Drilling (ICHD) method was used for residual stress analysis. Residual stresses were introduced in the samples by depositing one or two layers, with different clamping configurations. The measured residual stresses together with the observations noted during the experiments were analysed, compared, and discussed. The results show that double layer deposition can reduce residual stress gradients and provide a more stable stress profile along the thickness of the deposited layer. Furthermore, although single-sided clamping allowed for a higher freedom of thermal expansion and contraction during the deposition process, which leads to a more balanced stress distribution, it also increases deformation. Therefore, the use of uniform clamping during deposition of Stellite 6 should be implemented for actual application case. Additionally, depending on the desired thickness of Stellite 6, a multi-layer deposition strategy can be implemented to minimize residual stress build up.

The research concluded that defect-free Stellite 6 layers can be successfully deposited using the GMAW-based WAAM process. The residual stress measurement showed that preheating and reducing the thermal gradient can effectively reduce the residual stress within the deposited material. The obtained results can be helpful for the further development of automated toolpath generation and the integration of 3D vision control systems for more efficient and reliable WAAM processes.

Table of Contents

List of Figures

List of Tables

List of Abbreviations

AM	Additive Manufacturing
CAD	Computer-Aided Design
CMT	Cold Metal Transfer
CW-GMAW	Cold-Wire-Gas Metal Arc Welding
DED	Directed Energy Deposition
DLD	Direct Laser Deposition
FEA	Finite Element Analysis
GMAW	Gas Metal Arc Welding
GTAW	Gas Tungsten Arc Welding
HVOF	High-Velocity Oxyfuel
ICHD	Incremental Central Hold Drilling
LM	Layered Manufacturing
MAG	Metal Active Gas
MIG	Metal Inert Gas
PAW	Plasma Arc Welding
PTA	Plasma Transferred Arc
RP	Rapid Prototyping
SEM	Scanning Electron Microscope
SFF	Solid Free-Form Fabrication
WAAM	Wire Arc Additive Manufacturing

1. Introduction

The background of this research work is presented in this chapter, which includes section 1.1 presenting an overview of the fundamental concepts of Additive Manufacturing, focused on Wire Arc Additive Manufacturing (WAAM). It then delves into Gas Metal Arc Welding, a technique in WAAM families in section 1.2, which will be the technique used in this thesis work. Following, the section 1.3 introduces the properties and applications of Stellite 6 alloy. Section 1.4 describes the concept of residual stress, an important phenomenon occurring during manufacturing processes. Finally, section 1.5 introduces the motivation behind this research and provides an overview of the thesis structure.

1.1. Wire Arc Additive Manufacturing (WAAM)

The ASTM-F42 Committee defines Additive Manufacturing (AM) as a process that constructs objects from 3D model data by joining materials layer by layer [1]. In the commercial sector, AM has been known by various names, including three-dimensional (3D) printing, rapid prototyping (RP), layered manufacturing (LM), and solid free-form fabrication (SFF) [1]. Essentially, AM directly produces a near-net-shape 3D designs from a computer-aided design (CAD) file, eliminating the need for custom tools or molds for each part. This process involves sequentially building layers in the X-Y plane, which stack to form the Z or third dimension [1].

Additive manufacturing technologies have advanced quickly from their origins in prototyping to becoming effective methods for rapid manufacturing. Over the past ten years, significant improvements in deposition speed, accuracy, and material properties have made it possible to produce end-use parts with high density and excellent mechanical properties. Compared to traditional subtractive manufacturing methods, these technologies offer several benefits, including product customization and the elimination of tooling requirements for production [2].

Metallic AM techniques can be categorized based on the type of feedstock materials and energy sources used. Common feedstock materials in metallic AM include powder and wire. The use of wire as a feedstock material in metal AM has demonstrated potential for improving surface finish, enhancing material quality, and achieving higher deposition rates for large structures of moderate complexity. Additionally, wire-based techniques improve process efficiency and create a cleaner working environment, as the entire wire fed into the melt pool with barely loss in spatter and marginal loss in vaporization when process is working with optimal conditions, unlike powder-based techniques, where a significant portion of the powder often remains unmelted even at optimized condition [3]. The primary energy sources for wire deposition include electric arc, electron beam, and laser [4].

Metallic AM processes predominantly use fusion-based techniques, particularly in powder-bed systems that rely on laser or electron beam as heat source. While these methods offer high dimensional precision, they have low deposition rates, leading to longer production time. Furthermore, the use of powder feedstock materials can increase the possibility of defects, such as pores, which can weaken the integrity of parts, especially under dynamic loading conditions. In contrast, WAAM may not achieve the same precision as powder-bed systems, but it offers significantly higher deposition rates, allowing for the rapid production of large metallic structural components while maintaining

satisfactory quality. Both academic and industrial sectors are showing increasing interest in WAAM due to its economic and technical benefits [5].

WAAM is classified under ASTM F2792-12a as a direct energy deposition process [6]. It combines an electric arc as a heat source with a wire as the feedstock material, drawing from principles found in automated welding processes like Gas Metal Arc Welding (GMAW), Plasma Arc Welding (PAW), and Gas Tungsten Arc Welding (GTAW) [5]. The following section will provide a more detailed review of GMAW as it will be the basic technique used in this thesis.

1.2. Gas Metal Arc Welding based WAAM

Gas Metal Arc Welding (GMAW), also referred to as Metal Inert Gas (MIG) or Metal Active Gas (MAG) welding, is a fusion-based arc welding technique that is evolved into WAAM. In GMAW, an electric arc is generated between the end tip of a consumable wire and the workpiece, with the process protected by an inert or active shielding gas that protects the weld pool and surrounding material. Common shielding gases used in MIG welding include argon, helium, or a mixture of both. In MAG welding, carbon dioxide is often used, along with mixtures of argon or helium and gases such as CO_2, O_2, H_2, N_2, or NO to improve the process stability [7].

The GMAW based WAAM is attractive as its efficiency and versatility across various applications. The other two arc welding methods, GTAW and PAW, share a common feature in that both utilize a non-consumable tungsten electrode to create an electric arc with the workpiece, all under an inert shielding gas, and do not require filler material to be an electrode. GTAW is recognized for its precision and low defect rates due to its stable arc and often operating at low welding speed together with an external wire feeding system. PAW is a high-energy-density process in which the arc is confined by a nozzle, increasing its stability. PAW produces a highly concentrated ionized plasma with elevated temperatures and energy, making it a high-density energy process. Although its energy density is lower than that of laser-based techniques, it surpasses that of other electric arc processes [5].

Arc-based welding techniques are complex, requiring careful control of numerous process parameters to ensure optimal performance resulting good quality weld. These process parameters consist of current, voltage, wire feed speed, travel speed, shielding gas composition and flow rate, contact tip-to-work distance and torch angle [5]. The appropriate selection of these parameters influences the molten metallic droplet transfer mode, which is critical for determining bead shape, penetration, deposition rate, and surface roughness. To improve the molten metal deposition with lower heat input, a variation of GMAW, known as controlled short circuiting metal transfer, has been developed and adapted for additive manufacturing [5]. This type of metal transfer is referred to by various branch names like for instance Cold Metal Transfer (CMT) and surface tension transfer (STT).

1.3. *Overview of Stellite 6 Alloy*

Cobalt-based alloys, such as Stellite 6, are recognized for their exceptional resistance to wear, resistance to high temperature oxidation, thermal fatigue, and corrosion, making them attractive to be applied in challenging environments such as aerospace, industrial gas turbines, and nuclear applications [8]. It is also the material will be deposited in this thesis work. Apart from the Co base metal, Stellite 6, is composed of approximately 29 wt.% Cr, 4.5 wt.% W, 1.1 wt.% C, offers a well-rounded combination of strength, corrosion resistance, wear resistance, and thermal stability up to 500°C, which has been well studied [9].

Cobalt alloys, with additions of Tungsten (W), Molybdenum (Mo), and Carbon (C), present a wide range of properties. The differences in cobalt alloys are primarily due to variations in their chemical composition, especially in the amounts of Cr, W, and C, which significantly influence their performance and mechanical characteristics. Chromium plays a crucial role in strengthening the alloy by promoting the formation of Cr-rich solid solutions and carbides (M_7C_3 and $M_{23}C_6$), thereby enhancing resistance to corrosion, wear, erosion, and oxidation within the Co matrix [9]. Carbon increases hardness and wear resistance by encouraging the formation of strong carbide phases. Cobalt alloys with higher carbon content are typically used in applications requiring high wear resistance. Tungsten and Molybdenum act as refractory elements, further reinforcing the alloy by forming solid solutions, Mo-rich and W-rich carbides (MC and M_6C), and dispersed intermetallic phases within the Co-Cr matrix [9].

Stellite is often applied as a wear resistant coating. The hardfacing process plays an important role in the final coating surface performance. Optimal process parameters ensure strong bonding between the coating and substrate with minimal porosity, no cracking, and low dilution [10]. Several hardfacing techniques, including supersonic laser deposition, laser cladding, plasma transferred arc welding (PTAW), GMAW, GTAW, high velocity oxyfuel spraying (HVOF), cold spraying, and plasma spraying, have been used to process cobalt alloys, particularly Stellite 6. Each technique has its own advantages and disadvantages, which influence its suitability for industrial applications based on factors such as manufacturing requirements, time, and cost [9]. In Chapter 2, Section 2.1, a more in-depth discussion of the existing research on additive manufacturing techniques involving Stellite 6 will be reviewed. The focus of this thesis work will be the processing of the Stellite 6 and its resulting residual stress using GMAW base WAAM.

1.4. *Fundamental of Residual Stress*

Residual stress generally refers to internal stresses that remain in a material after it has been subjected to manufacturing processes such as welding, casting, or machining [11]. It can also arise from in-service repairs or modifications [11], even in the absence of external forces [12]. These stresses arise due to non-uniform plastic deformation, phase transformations, or temperature gradients during processing [13]. Understanding residual stress is important because it can have an influence on the mechanical properties of materials, such as fatigue life, fracture toughness, and dimensional stability [12].

Residual stresses refer to the internal stresses present within a material when no external loads or thermal gradients are applied. The residual stresses existing in a material are stationary and are in equilibrium with surrounding. It can severely affect the material's performance or significantly reduce the component's life. The residual stresses may be categorised according to characteristic length scales [12]. Macro and micro residual stresses are two primary categories of residual stress. Macro residual stresses occur over large distances within a component. They can be resulted from thermal gradients or mechanical loading during manufacturing processes. In contrast, micro residual stresses exist on a much smaller scale, typically within individual grains, and arise from variations in the microstructure, such as differences in thermal expansion coefficients between phases in a composite material [12].

As materials experience different thermal cycles during the deposition using WAAM, stresses develop within the deposit and substrate materials. Compressive stress is introduced during the heating cycle in the substrate. Tensile stress is introduced during the cooling cycle in the substrate. Depending on the difference in thermal expansion coefficients of coating and substrate material (thermal mismatch), tensile or compressive stresses will be introduced in the deposited layers as a result from different thermal gradient were introduced during the deposition process. The accumulative strain remains after cooling of the material is completed and leads to residual restress within the material. Since tensile residual stresses influence wear and corrosion resistance as well as the resistance against static and dynamic loading negatively, it is of primary importance to know how different processing conditions influence the residual stresses [14]. The high cooling rates, non-linear properties of the materials at elevated temperature and differential shrinkages involved in the WAAM are responsible for such tensile residual stresses, which may exceed the yield strength of the deposited material resulting in cracking and/or deformations [3].

The measurement of residual stress is challenging because it cannot be directly observed [12]. Instead, various indirect methods have been developed, classified into non-destructive and locally destructive techniques. Non-destructive methods include X-ray diffraction, neutron diffraction, and ultrasonic techniques, which detect stress through changes in crystal lattice spacings or wave propagation characteristics. Locally destructive methods involve techniques like hole drilling and layer removal, where material is removed to allow stress relaxation, and the resulting deformation is measured to determine the initial stress distribution [15].

Each measurement method has its advantages and limitations. On one hand, non-destructive methods are preferred for their ability to assess stress without damaging the material, but they often require sophisticated equipment and may be limited in measurement depth. On the other hand, locally destructive methods, while more disruptive, are often simpler and less expensive but may introduce additional errors due to material removal [15]. Understanding the principles behind these methods and choosing the appropriate one based on the specific application is important for a good residual stress assessment. In Chapter 2, Section 2.2, a more detailed review of the existing research on residual stress will be presented.

1.5. *Motivation and Thesis Structure*

As industries increasingly focus on sustainability and the low production with high efficiency and satisfactory mechanical properties, GMAW based WAAM has appeared as a promising and viable approach among all the techniques mentioned in the earlier sections. Many current research focused more on 3D printing using GMAW based WAAM rather than the regeneration and hardfacing that this technique also offered. As commonly known by the welding community that excessive arc energy can be generated during GMAW welding. This can lead to residual stresses build up that sometime cannot be fully mitigated by post heat treatments. However, in the literature the effects of residual stresses are not commonly addressed as most researchers [3,16-19] focus on process optimization or investigate the coating properties. Less attention was made for investigating the residual stresses induced by material processing. Without a good understanding of the residual stress build up during the WAAM deposition of the superalloy like Stellite 6, it will be challenging to design a proper toolpath for hardfacing a large component. The introduction of residual stresses may even lead to a reverse effect instead of improving the surface performance. Residual stress is a complex subject to be fully investigated during a short period of time such as this thesis work. However, this project was set up according to the industrial actual application, where deposition Stellite 6 on a stainless steel 316L substrate was performed, in which the residual stress development during its application is not fully clear and fundament study needs to be carried out to help for better clamping design. Based on their manual operation experience, this thesis work will help the interested industrial partner to gradually transition from manual operation towards a semiautomatic GMAW based WAAM operation. Although this thesis work merely scratchs the surface of the subject, but it aims to provide a foundation for further development of the automatic toolpath generation based on the 3D vision monitoring and control system [20], in which toolpath sequencing, segmentation and interpass temperature control will need to be considered. These are not in the scope of this thesis work. This thesis work also aims to contribute to the broader goal of improving the industrial application of WAAM, particularly in the repair and restoration of high-value components. The research outcomes will help for better toolpath design and sequencing when applying automated solutions for hardfacing Stellite 6 using WAAM, which is a common goal of the interested partner mentioned earlier. Due to confidential reason, the interested partner and the actual application background cannot be mentioned explicitly in this thesis work.

This thesis is structured into five main chapters. The Introduction provides an overview of WAAM, specifically focusing on GMAW and its application for Stellite 6 alloy deposition, while introducing the research motivation and objectives. The Literature Review explores previous research on hardfacing Stellite 6 and the development of residual stress, particularly focusing on deposition strategies and stress measurement techniques. The Experimental Setup and Methods chapter details the design and execution of the experiments, covering the materials, methodologies, and equipment used, with an emphasis on the Incremental Central Hole Drilling method for residual stress measurement. Results and Discussion follows, presenting the findings of the experiments, including finite element analysis of deformation and the residual stress analysis. Finally, the Conclusion and Future Work chapter summarizes the key outcomes of the research, discusses its implications for industrial applications of WAAM, and outlines potential directions for future study.

2. Literature Review

This chapter begins with a review of previous studies on Stellite 6 in section 2.1, followed by an exploration of the existing literature on residual stress in section 2.2. Subsequently, the influences of deposition strategies on resulting residual stress are reviewed in section 2.3. In section 2.4, the residual stress measurement techniques, with a particular focus on the hole drilling method for residual stress measurements, is reviewed.

2.1. Previous Hardfacing Research on Stellite 6

Recent studies have reviewed on various methods of Stellite 6 deposition and their analyses. Li et al. [21] deposited Stellite 6 on Stainless Steel 304L using GTAW based WAAM. The microstructure of the deposit was compared with the casted microstructure. Figure 1a and 1c show optical microstructure images, while figure 1b and 1d show SEM images, of the samples cut from the WAAM deposit and the casted part, respectively. Both methods resulted in a hypoeutectic structure featuring primary dendrites and interdendritic eutectics. The light region, consisting of the Co-rich γ solid solution (fcc), contains dendrites, while the dark interdendritic region is primarily made up of γ-Co along with M_7C_3 carbides (hcp), where M typically includes Co, Cr, and Fe. The microstructure in WAAM parts showed potential for enhanced mechanical properties due to carbide refinement and refined grain size, although the increased dendritic arm spacing may reduce hardness as a result of slower cooling rates during manufacturing [21].

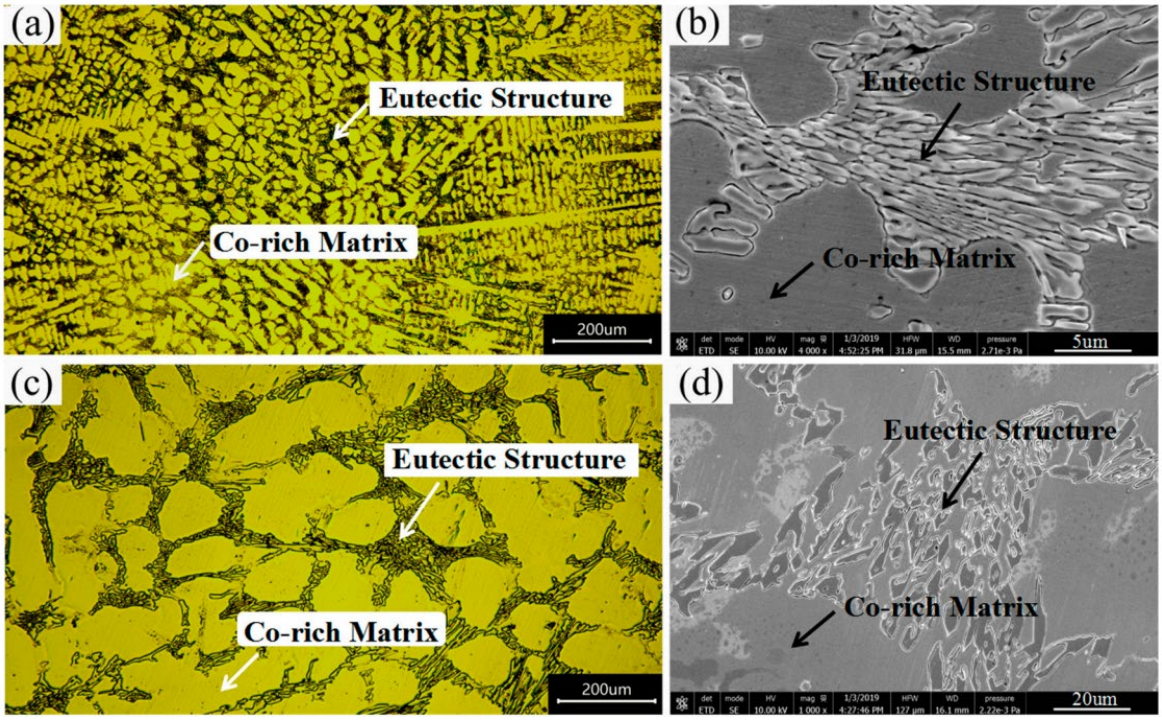

Figure 1. Optical (a,c) and SEM (b,d) microstructure images of the wire arc additive manufacturing Stellite 6 part (a,b) and casted part (c,d) [21].

Toozandehjani et al. [9] focused on high tungsten (6 - 8 wt.%) Stellite 6 coatings applied to St37 and Mo40 steel substrates using a twin hot-wire arc welding technique. Their findings showed that these coatings achieved strong bonding, with fine dendritic microstructures. This was especially the case when deposited on the St37 substrate maybe due to higher cool rate that was induced. This finer structure, combined with a higher tungsten content and lower iron dilution, resulted in improved hardness and wear resistance [9].

Gholipour et al. [22] investigated a Stellite 6 cladding on 17-4 PH stainless steel using GTAW. They observed that solidification began with the formation of a Co solid solution, transitioning through different microstructural stages from cellular to equiaxed dendrites as cooling rates increased. During later stages, the interdendritic melt, enriched with carbon and chromium, approached the eutectic composition, leading to the formation of eutectic $(Cr,Co)_7C_3$ carbides. Figure 2 shows the optical observations across various stages of solidification [22].

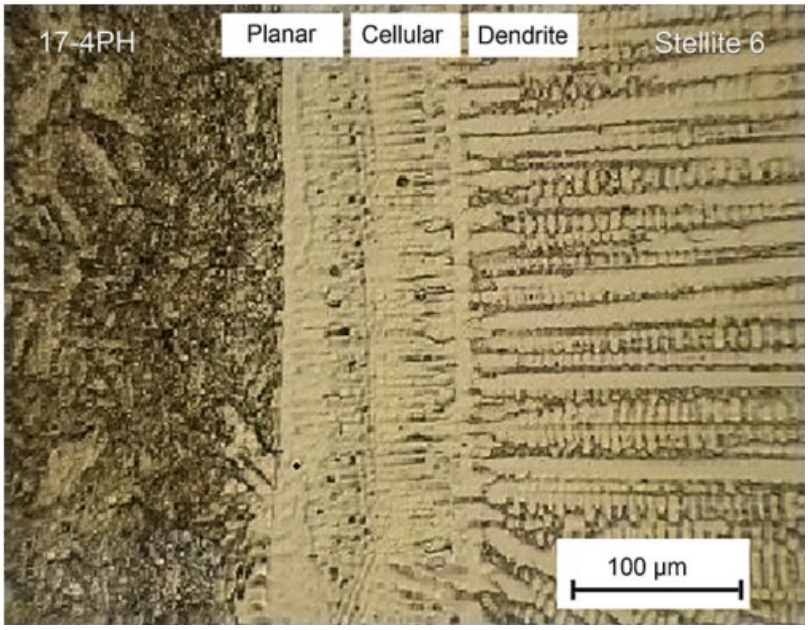

Figure 2. Optical micrograph showing different stages of solidification [22].

Khouzani et al. [23] reported the effects of spark plasma sintering (SPS) of Stellite 6. They found that while complete elimination of porosity was not achievable, minimal porosity (about 3%) and high densification occurred at 1050 °C after 10 minutes of sintering. However, extended sintering times resulted in coarsening of chromium carbides, while lower temperatures led to incomplete sintering [23].

In a study done by Rajeev et al. [16], the performance of Stellite 21 hardfacing on H13 steel was compared using CMT and PTAW processes. The aim was to examine how these processes impact microstructure, dilution, and wear behaviour. The findings revealed that CMT produced a finer microstructure and lower dilution than PTAW, leading to better wear resistance at both room and high temperatures. This improved performance is attributed to the lower heat input of the CMT process, resulting in finer dendritic structures, which enhanced the coating's hardness and durability [16].

Silva et al. [17] evaluated the cavitation erosion resistance of coatings made from austenitic stainless steel and cobalt alloys (Stellite 21 and Stellite 6) using GMAW and Cold-Wire-Gas Metal Arc Welding (CW-GMAW) processes. The aim was to assess the durability of these coatings under cavitation conditions, commonly employed in hydraulic systems. The study found that cobalt alloys, especially Stellite 6, demonstrated significantly better cavitation resistance compared to austenitic stainless steel, reducing mass loss by around 90%. The CW-GMAW process provided similar resistance to cavitation as GMAW but at a lower production cost, making it a promising option for industrial applications such as turbine repairs. This was due to the microstructural features and phase transformations observed in the coatings during wear testing [17].

In a study by Murugan et al., [18] the fabrication of Stellite 6 alloy prototype parts using Robotic WAAM with the CMT process was investigated. The aim was to assess the microstructural and mechanical properties of Stellite 6 and determine its potential for high-strength, complex parts. Cracks were observed in the plate after 42 layers, which were linked to the build up of residual stress from solidification shrinkage. However, by applying preheating, stress-relieving, and post-heating techniques, cracking was successfully prevented in the cylindrical parts. The results showed improved mechanical properties, with the plate exhibiting higher tensile strength and hardness compared to the cylinder. This difference was attributed to variations in cooling rates, affecting the microstructure and dendrite formation during the deposition process [18].

All studies mentioned before show that Stellite 6 has been studied with different material processing techniques aiming to have good bonding and maintaining the integrity of Stellite 6. The cooling rate has an effect on the resulting microstructure. Satisfactory Stellite 6 hardfacing deposits can be developed with different techniques as reported in the literature and it can be even further enhanced with addition of high melting point element such as tungsten. Little has been reported on processing Stellite 6 using GMAW based WAAM. Lin et al. [19] was able to optimize the GMAW based WAAM to produce crack free and dense Stellite 6 coatings using the strategy of straight line deposition with alternating directions. It is, however, not indicated how much the deposition strategy influences a successful deposition. This is one important aspect as not all industrial components can be made with the straight line strategy [19]. In any case, the deposition of Stellite 6 using GMAW based WAAM is achievable and low heat input of GMAW based WAAM will be aimed in this thesis work.

2.2. Previous Research on Residual Stress Induced during Stellite 6 Deposition

Little research has been reported in the literature on subjects related to residual stress during deposition using GMAW based WAAM. The literature related to the hardfacing of Stelite 6 using other heat sources were reviewed in the following. The quality of laser hardfaced Stellite 6 was referenced as one of our research targets to achieve Stellite 6 hardfacing using a GMAW based WAAM system. One of the targets is to achieve Stellite 6 hardfacing with as low heat input as possible.

Ya's [3] investigation into residual stresses in Stellite 6 layers cladded on AISI 420 steel plates using a Nd:YAG laser revealed that optimal process parameters can produce cladding with satisfactory properties, such as geometry, dilution, and hardness. Challenges like cracking and deformation were attributed to tensile residual stress that had developed during the cladding process. The study examined

different strategies to decrease these stresses, including preheating the substrate (figure 3), using intermediate layers (figure 4), and adjusting energy input (figure 5). The findings showed that preheating had the greatest impact on reducing residual stress, followed by modifying energy input and the use of intermediate layers. Figure 6 shows that residual stresses in clad layers were measured using layer removal and hole drilling techniques, for both methods he reported that the residual stress measurement were in a good agreement as shown in figure 6. The highest stresses were observed near the clad/substrate interface, with stresses being higher along the cladding direction [3].

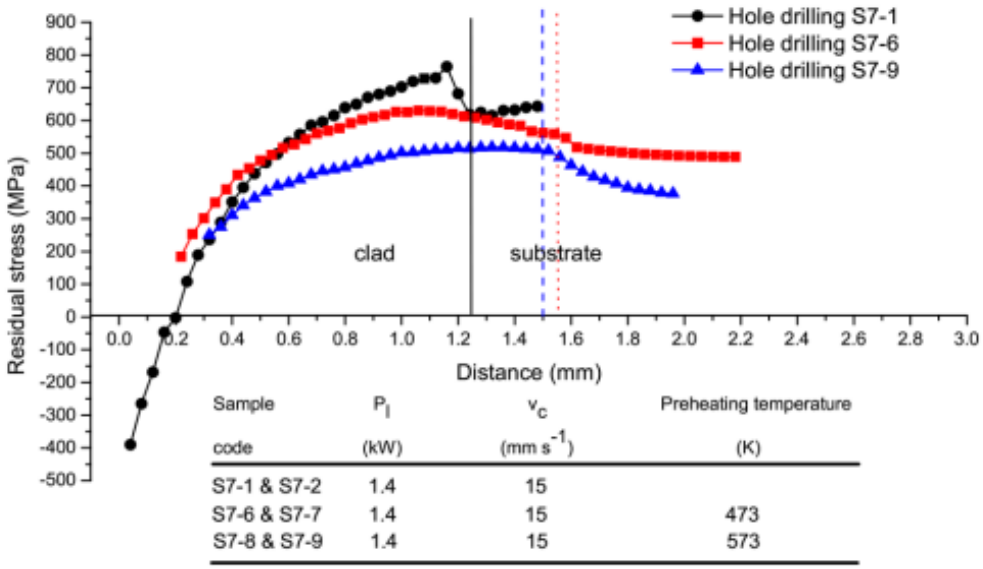

Sample code	P_l (kW)	v_c (mm s^{-1})	Preheating temperature (K)
S7-1 & S7-2	1.4	15	
S7-6 & S7-7	1.4	15	473
S7-8 & S7-9	1.4	15	573

Figure 3. Influence of preheating on residual stresses. Residual stress values were 764 MPa for Sample S7-1 (No preheating), 630 MPa for Sample S7-6 (Preheated to 473 K) and 518 MPa for Sample S7-9 (Preheated to 573 K) [3].

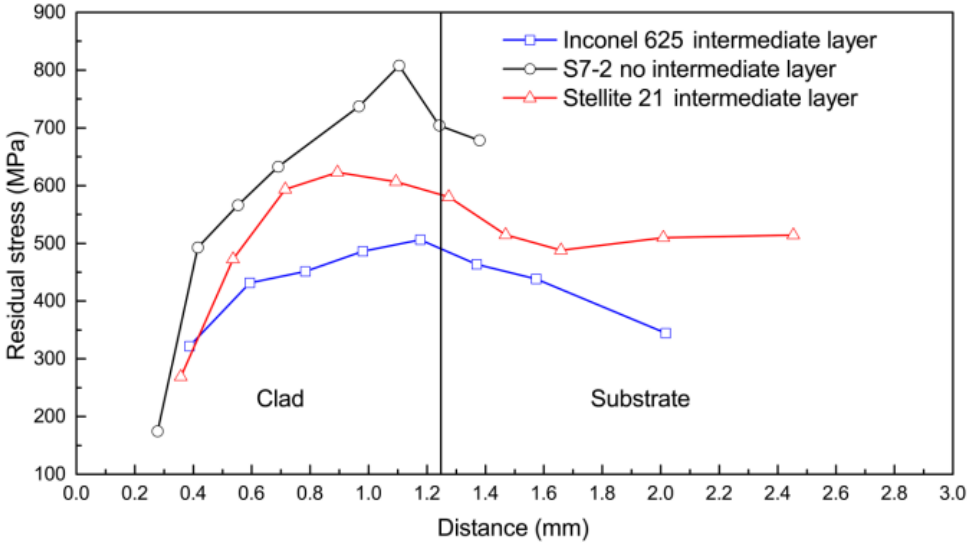

Figure 4. Effect of Intermediate Clad Layers (Stellite 21 and Inconel 625) on Residual Stresses [3].

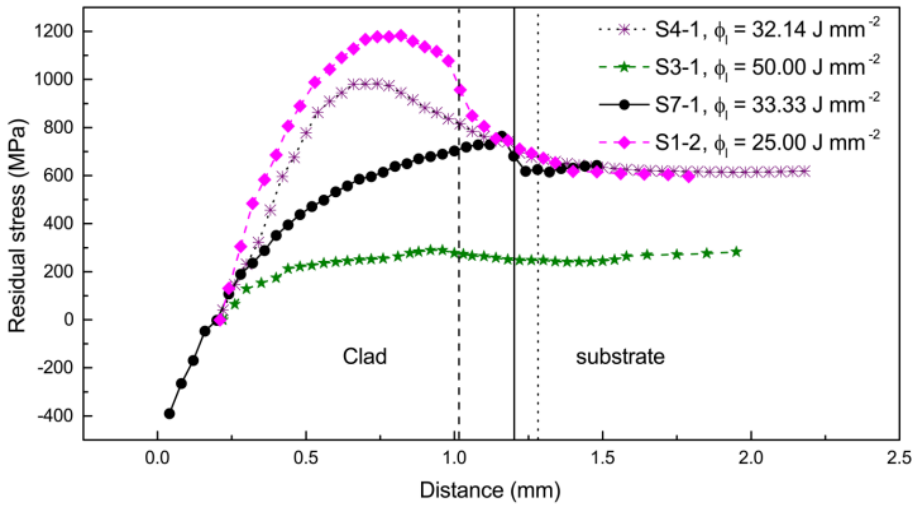

Figure 5. Influence of Effective Energy Input on Residual Stresses. Sample S3-1, which was produced with the highest effective energy input, shows the lowest residual stress level [3].

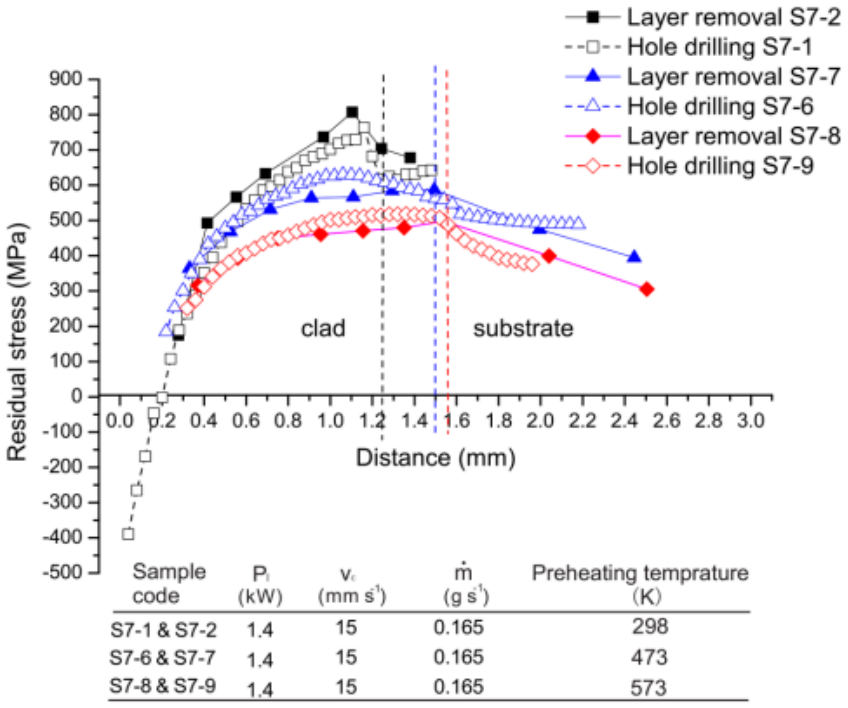

Sample code	P_l (kW)	v_c (mm s^{-1})	$\dot{m}$ (g s^{-1})	Preheating temprature (K)
S7-1 & S7-2	1.4	15	0.165	298
S7-6 & S7-7	1.4	15	0.165	473
S7-8 & S7-9	1.4	15	0.165	573

Figure 6. Comparison of residual stresses (σ_x) assessed using layer removal and hole drilling methods [3].

Pilehrood et al. [24] studied the role of residual stress in solidification cracking during the Laser Metal Deposition (LMD) process/laser cladding. The research identified thermal gradients as the primary cause of residual stress, influenced by factors such as poisson's ratio, elastic modulus, and thermal expansion coefficients. Reducing temperature differentials was suggested as a key strategy to prevent solidification cracking, as thermally induced residual stress significantly contributes to crack initiation. Additionally, the study highlighted the effectiveness of increasing deposition speed to reduce both thermal residual stress and dilution, thereby minimizing the risk of cracking [24].

Thawari et al. [25] focused their study on the impact of laser cladding parameters on distortion and thermal history. Their findings showed that thermal gradients and rapid temperature fluctuations during the process contribute to permanent deformations, with lower scan speeds and higher laser power leading to increased deflection. The study also noted that lower distortions occurred during the deposition of subsequent layers in multi-layer cladding [25].

Guo et al. [26] examined residual stress distribution in Stellite 6 cladding on 420 steel steam turbine blades. Using blind-hole drilling and digital image correlation methods, they found that despite a stress relief through heat treatment, the cladding layer retained in tensile stress, ranging from 200 to 300 MPa, while the substrate exhibited a compressive stress between -100 and -150 MPa. The study concluded that a significant residual stress gradient exists at the interface between the cladding layer and substrate, with higher residual stress values near the fusion boundary compared to other locations as shown in figure 7 [26].

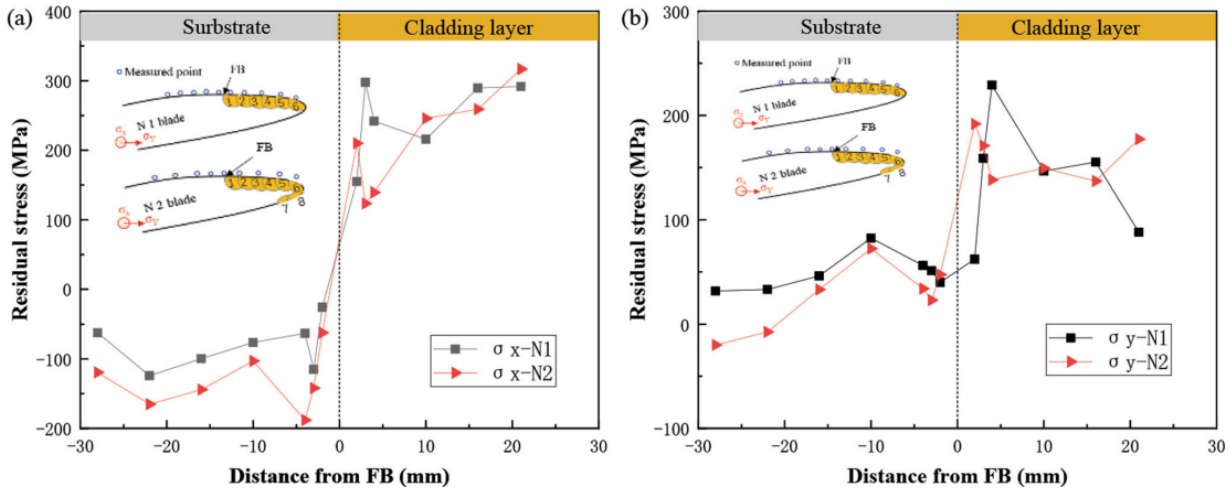

Figure 7. Distributions of residual stresses of the cladding layers on the convex sides of Line 3 in blades N1 and N2 (a) σ_x; (b) σ_y [26].

The results mentioned above shows that the highest residual stress builds up occurs at the interface between the Stellite 6 and substrate. This is to be expected as this is the region where the thermal mismatch between the two different materials occurs. Although, there is mixing between the materials during the fusion bonding process, the difference between the materials will still exists. By understanding this, it can help to better design the deposition produce in practical applications when different deposition strategies could be employed

In a study conducted by Leggatt [27], one of the primary factors influencing residual stresses in welded structures is the application of restraints during the welding process. These restraints can take the form of external fixtures, such as welding jigs or local alignment tools, as well as from the attachment of parts to other components of the structure through welding or tacking. The study also emphasizes a wide range of factors that can alter residual stresses after welding, either during subsequent manufacturing stages or throughout the service life of the welded structure. A notable example of a manufacturing operation that can significantly modify the residual stresses in a welded structure is the release of temporary fixtures [27].

Considering the deposition using GMAW based WAAM, the substrate already can be locally preheated by the arc. The excessive heat generated by arc and accumulated in the substrate can raise the substrate temperature quickly. Preheating substrate will not be used in this thesis, which also requested by the industrial partner. Additionally, the experimental design in this thesis work will be focusing more on the release of temporary fixtures, with the goal of evaluating the differences in residual stress levels before and after the removal of clamps as this information will help for better design for clamping

2.3. *Influence of Deposition Strategies on Residual Stress*

Path planning (or toolpath design) is a crucial aspect when deposition metallic material using WAAM. A good tool path planned can improve deposited surface quality and deposition accuracy. This is currently programmed based on operation experiences. Residual stress developed during deposition using WAAM is expected to be influenced by various factors, including power source (type of material transfer mode used), deposition parameters, strategy, speed, layer thickness, and substrate material [28]. The material deposition process involves localized heating and uneven cooling, leading to significant thermal gradients that result in residual stress and distortion. These effects can weaken structural integrity and affect the final geometry of the part. WAAM tool path planning includes build orientation, path sequencing together with the suited process parameters, all of which must be carefully managed to avoid large residual stress build up, especially when depositing a large structure. The substrate used for deposition frequently experiences distortion. This distortion can be minimized by depositing WAAM layers on both sides of the substrate, which helps balance the deformation caused by residual stresses on each side. This often is not practical when depositing structure that is not symmetrical and depositing without an external positioner. An appropriate deposition strategy can also aid in controlling the development of residual stresses. A number of tool path planning strategies exist for WAAM such as raster, zigzag, etc [28]. A unidirectional path pattern is commonly used in WAAM In this thesis work, zigzag toolpath was interested as the project wished to start as close as the manual operation that zigzag deposition was done manually. Hence, this review is more focused on the existing research that related to use the zigzag toolpath for deposition.

Lin's [29] study utilized WAAM for the deposition of AM-XC-45 (medium carbon steel) and Stellite 6. It highlights several features of zigzag path planning, reduction in the number of start and stop points, increased efficiency due to the combination of lines. There is however a drawback of poor outline accuracy of the part leading to a rough surface finishing [29].

In a study carried out by Ahmad et al., [29] residual stress is compared among three different deposition strategies when depositing Ti_6Al_4V using WAAM, which included single bead, parallel path (deposition direction parallel to the long edge of the deposit), and oscillation (zigzag) path (deposition direction starts along short edge of the deposit), as shown in figure 8a. It shows that all three strategies result in stress distribution characterized by high tensile stresses at the top and bottom of the walls. The contour method was used for the residual stress measurement. The oscillation path wall shows the lowest residual stress (<100 MPa), while the parallel path wall shows the highest residual stress, with peak tensile stress reaching 200 MPa at the top of the wall. In contrast, the maximum tensile stress in the single bead wall is around 185 MPa, located near the bottom of the wall, as shown in figure 8b. This lower stress in the oscillation path is due to its shorter deposition paths, resulting in a less steep thermal gradient compared to the other two deposition strategies [29].

According to Ya's [3] study, the most effective method to control residual stress is by preheating. The zigzag path results in the lowest residual stress when the substrate is consistently preheated through the continuous arc, which helps to naturally reduce residual stress build up. This is consistent with Thawari et al.'s [25] findings, where preheating during deposition lowers the thermal gradient and minimizes residual stress.

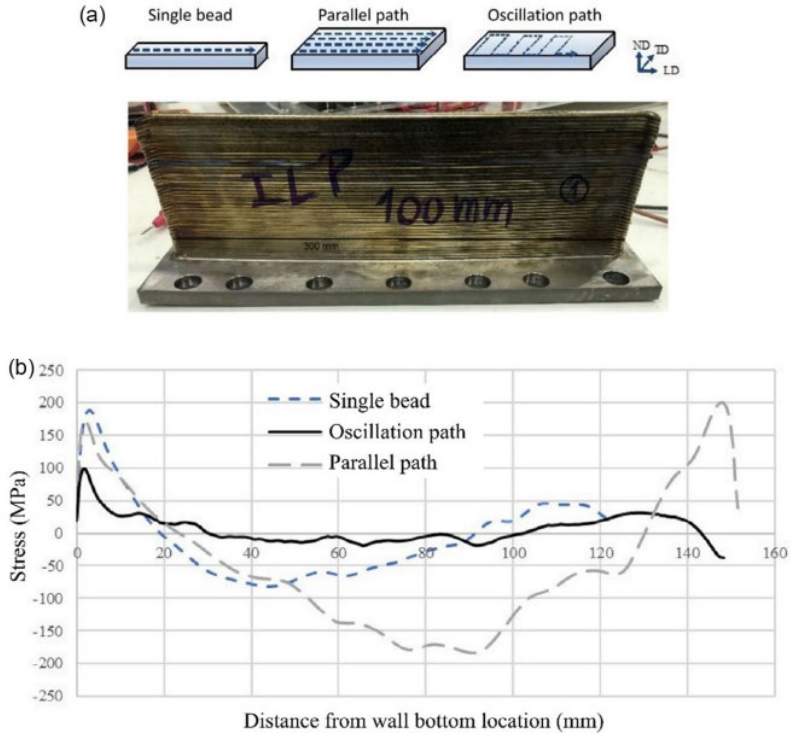

Figure 8. Residual stress distribution in WAAM Ti_6Al_4V walls under three different scanning strategies. a) Schematic of the deposition strategies: single bead, parallel and oscillation path, a WAAM deposited wall (wall thickness = 10, 25, and 20 mm for single bead, parallel, and oscillation path, respectively), where build direction is parallel to normal direction (ND) direction, and b) measured RS along build direction at mid-wall thickness after being removed from the substrate [29].

In multi-track multilayer DMD processes, Ghosh and Choi [30] proposed that the existing numerical model should incorporate phase transformation plasticity to improve the accuracy of residual stress predictions. A similar approach is suggested in a study on fabrication of EH36 steel using WAAM, where accounting for phase transformations in simulations is recommended when dealing with complex deposition patterns. Complex deposition patterns refer to deposition paths or toolpaths that involve more intricate, non-linear, or multi-directional movements of the WAAM tool. These paths are not straightforward linear movements. Instead, they include patterns like zigzag, raster, spiral (in-out and out-in), and alternate. Figure 9 shows the predicted Mises stress distributions, both with and without considering phase transformation, along the diagonal of WAAM-produced EH36 steel under five different deposition patterns. The results indicate that residual stresses might be underestimated if phase transformation is neglected, particularly in continuous toolpath patterns like zigzag, in-out, and out-in. The zigzag deposition toolpath pattern shows the lowest Mises stress, while the out-in pattern exhibits the highest [28].

Additionally, Amine et al. [31] examined the impact of scanning directions on residual stress using the FEM approach. Their model, however, showed no significant differences in residual stress effects between parallel laser scanning paths and zigzag paths [28]. This may be due to the fact that both deposition strategies resulted in similar thermal behaviour during the direct laser deposition process (DLD). In both parallel and zigzag paths, the repeated reheating and remelting of layers create comparable thermal gradients and cooling rates, which are the primary drivers of residual stress build up. Since both patterns involve multiple layers experiencing similar thermal cycles, the overall heat distribution and dissipation across the material are effectively uniform, leading to similar residual stress levels. Therefore, any differences in the deposition direction are not significant enough to alter the thermal history or the big difference resulted in the residual stress patterns.

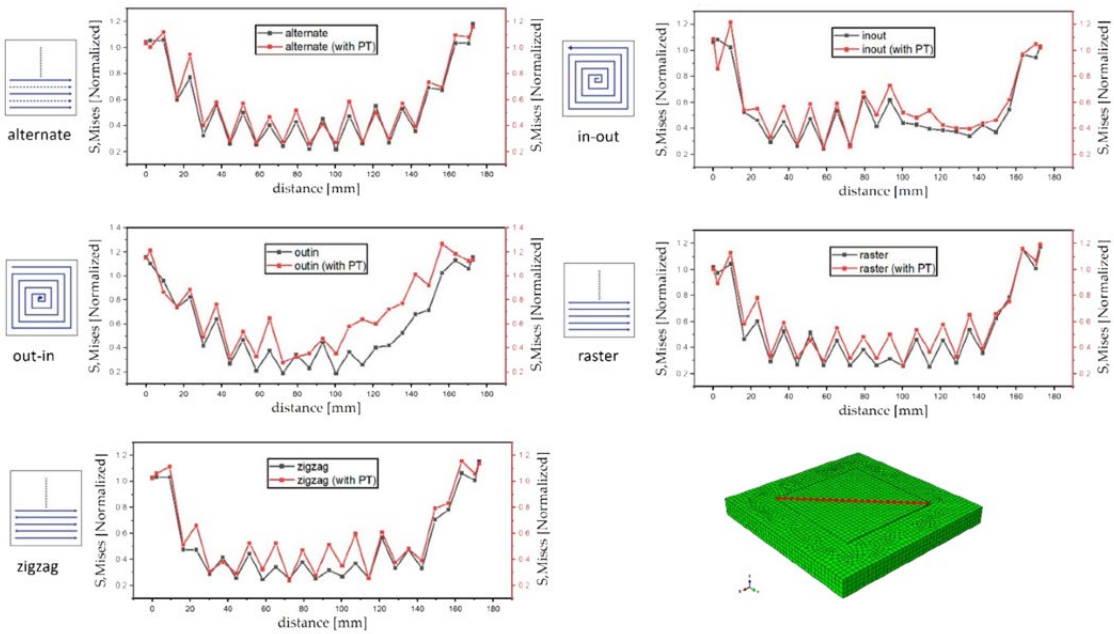

Figure 9. Effect of phase transformation on RS modelling for DED processes. Predicted Mises (residual) stress distributions with and without phase transformation along the diagonal of WAAM-produced EH36 steel under five deposition patterns [28].

In a FEM study of WAAM performed by Sun et al., [32] using aluminium alloy AA2319, an S-pattern (shown in figure 10a), which consists of variable line segments and allows generation a weave structure among layers, is found to be the optimum deposition pattern for the process that can achieve the lowest value of both equivalent and maximum principal residual stress, as compared to five others mostly adopted patterns (zig-zag, raster, alternative-line, in-out spiral, and out-in spiral). Due to the combined use of adjustable-length deposition paths as well as alternate of deposition paths directions, the S pattern produces a stress field with the most uniformity, as shown in figure 10b-d [28].

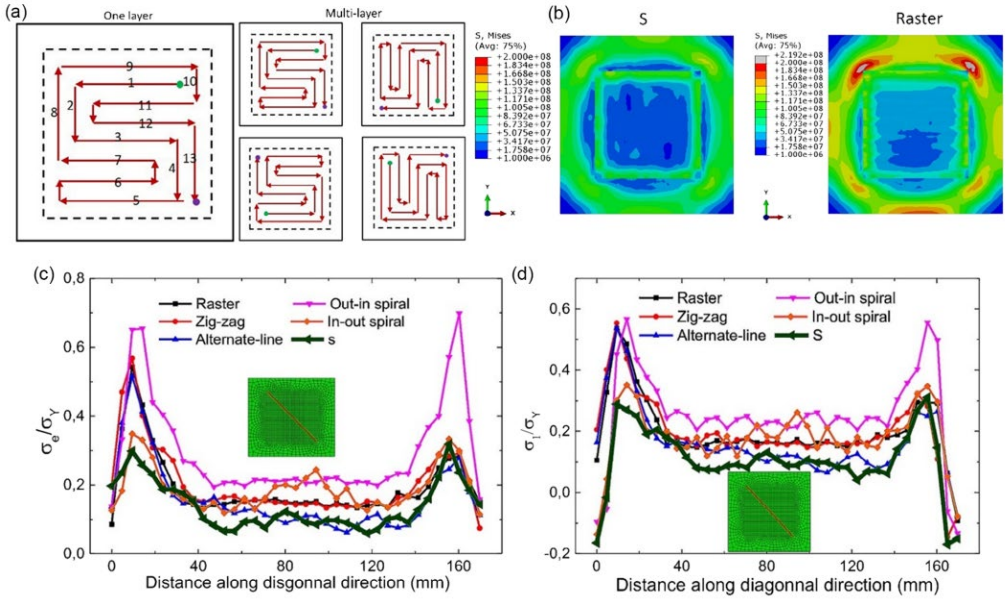

Figure 10. 3D FEM analysis of RS under novel deposition patterns for WAAM process of aluminium alloy 2319. a) S pattern of one layer and multilayer consisting of multiple line segments and varied scan directions (green and blue dots indicate the start and end of a laser scan), b) top view of equivalent residual stress distribution in one-layer deposition simulation, c) comparison of normalized equivalent residual stress, and d) normalized maximum principal residual stress, along diagonal direction in the deposit surface [28].

In the study performed by Somashekara et al., [33] the effect of area filling in a twin-wire arc weld deposition process using ER70S-6 filler wire and a C45 steel substrate was investigated. Three area-filling patterns are compared (raster, spiral-in, and spiral-out as shown in figure 11) in terms of the effect on the residual stress developed. The residual stress is found to be the lowest for the raster pattern, followed by the spiral-in and spiral-out [33].

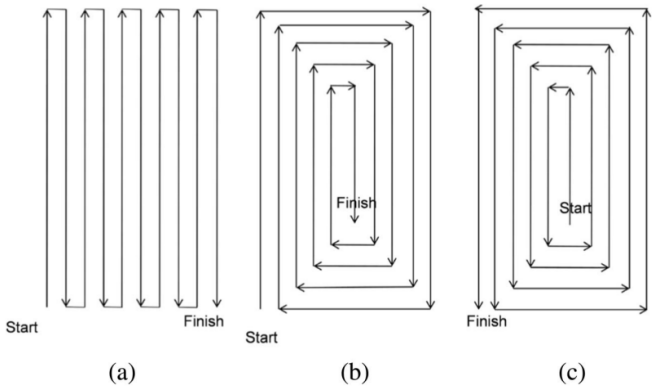

Figure 11. Three types of patterns used in weld-deposition are as follows: a raster, b spiral-in, and c spiral-out [33].

Given the various considerations after reviewing the literatures, the selection of the zigzag pattern for the deposition path of this thesis was driven by a combination of efficiency and its ability to moderate residual stresses. The zigzag pattern is expected to be able to achieve an optimal balance between practical deposition needs and stress management. It minimizes the number of start-stop points, which is crucial for maintaining consistent deposition quality and reducing manufacturing time for the intended industrial application. The zigzag pattern is expected to be able to generate a relatively uniform thermal gradient that can help to control the overall residual stress distribution effectively.

This makes it particularly interesting for the scenarios where a moderate level of residual stress is acceptable, and where the benefits of reduced complexity and higher efficiency in production are prioritized.

2.4. Measurement of Stress Using the Hole Drilling Method

As previously mentioned, measuring residual stress across all levels presents significant challenges since it cannot be directly measured [12]. In general strains are measured and stresses are calculated taking material properties into account Therefore, several indirect techniques have been developed to address this issue. One of the methods, is the localized destructive technique known as hole drilling [15].

In regions of a sample that remain undisturbed but possess residual stresses, machining will cause deformation, which can be analysed to back-calculate the residual stress profile. Typically, this involves drilling a hole and measuring the resulting strain in the surrounding area using various strain gauges, include strain gauge rosettes, as shown in figure 12 [34].

In the study conducted by Ya [3], residual stresses were calculated from the measured micro-strains using the following equations,

$$\sigma_{max} = \frac{\varepsilon_1 + \varepsilon_3}{4A} - \frac{1}{4B}\sqrt{(\varepsilon_3 - \varepsilon_1)^2 + (\varepsilon_3 + \varepsilon_1 - 2\varepsilon_2)^2} \quad (1)$$

$$\sigma_{min} = \frac{\varepsilon_1 + \varepsilon_3}{4A} + \frac{1}{4B}\sqrt{(\varepsilon_3 - \varepsilon_1)^2 + (\varepsilon_3 + \varepsilon_1 - 2\varepsilon_2)^2} \quad (2)$$

$$\tan 2\beta = {(\varepsilon_1 - 2\varepsilon_2 + \varepsilon_3)}\Big/{(\varepsilon_3 - \varepsilon_1)} \quad (3)$$

where σ_{max} and σ_{min} are the principal stresses, while ε_1 , ε_2 and ε_3 represent the strains recorded with gauges 1, 2, 3 which are aligned at 0°, 90° and 135° relative to the cladding direction. A and B refer to the gauge constants and β is the angle between the x direction and σ_{max} direction [3].

Although it is possible to determine the stress variation with depth by progressively deepening the hole, obtaining accurate measurements beyond a depth equal to the diameter is difficult as the type of used strain gauge cannot measure any strain variation after a certain distance. Furthermore, with a three-strain gauge rosette, only the two in-plane stress components can be measured. Despite this, the method remains economical and widely used [12]. Water jets [35] are sometimes chosen over mechanical drilling to reduce deformation that can be caused by machining. Although this method has been used to evaluate stress levels in coatings, it is not practical for very thin (<100 μm) or brittle coatings [12].

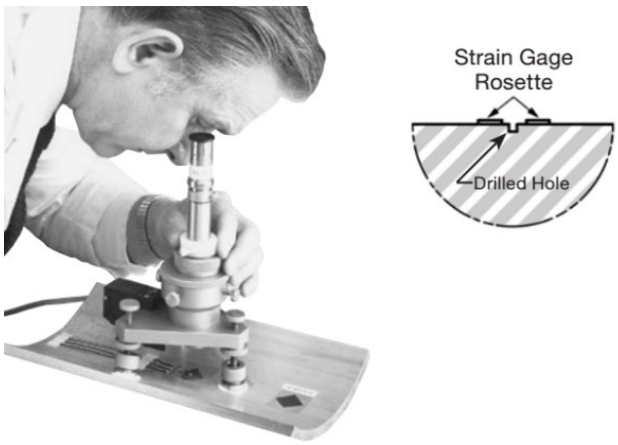

Figure 12. Hole Drilling Strain Gage Method [34].

The study performed by Yi and Park [36] focused on the residual stress analysis induced by GMAW in aluminium alloys commonly used in shipbuilding and offshore structures, specifically Al 5083, Al 6061, and Al 6082. The researchers developed a precise heat source model for GMAW using finite element analysis (FEA) to simulate the thermal and mechanical behaviour during welding. To validate the simulation, they conducted welding experiments and measured residual stresses using the hole drilling technique. The study's findings confirmed the accuracy of the heat source model by comparing the simulation results with actual thermal history and stress measurements, establishing its effectiveness in predicting welding-induced residual stresses [36].

The study performed by Farrahi et al. [37] investigated the residual stresses induced by MAG in St-37 steel plates. The researchers employed the centre-hole drilling method to measure residual stresses in welded specimens, analysing the stress distribution at the weld toe. Furthermore, the study incorporated a Genetic Algorithm (GA) to predict residual stress values based on experimental crack growth rates, achieving a good approximation of residual stresses without direct measurement. This approach enhances the ability to predict fatigue life in welded structures, making it a valuable tool in the management of welding-induced stresses [37].

The study performed by Ghosh and Ghosh [38] investigated the influence of pulse parameters on residual stresses in GMAW of high-strength aluminium alloys. The research focuses on how pulsed current GMAW affects the size of the weld and the resulting residual stresses, using a novel approach to analyse pulse parameters through a dimensionless factor. Residual stresses were assessed using the hole drilling strain gauge technique. Their findings show that adjusting the pulse parameters, including the pulse (peak) current, base current, pulse duration, and pulse frequency, can reduce both longitudinal and transverse residual stresses, improving the overall fatigue life of the weld joint [38].

All reviewed studies shown that the hole drilling method is a reliable approach for measuring residual stress of the deposit made using GMAW or GMAW based WAAM. This hole drilling technique has been widely used to assess stress distribution, with researchers highlighting its accuracy and effectiveness. For more validated results, the hole drilling method can be complemented by computational techniques such as FEA.

2.5. *Summary of the Literature Review and Motivation of this Thesis Work*

Based on reviewed literatures, it is clear that Stellite 6 can be processed using GMAW based WAAM with optimized process parameters. However, it was not reported in the literature how much residual stress can be developed when depositing Stellite 6 on steel or stainless steel substrate. It also known from the literature that the residual stress development can be associated with the type of toolpath pattern used for deposition. It was reported that the oscillation (zigzag) deposition will result in lowest residual stress and can be a viable solution for industrial production due to the features that it offers, which happens to be the manual operation that is currently used in the practice. Although methods to evaluate different levels of residual stress exist, it is still difficult to evaluate full scale of residual stress distribution experimentally. Considering the practical application of the depositing the Stellite 6 for hardfacing purposes, which is essentially is a thick layer coating process, the hole drilling technique will be most suitable for its resulted residual stress measurement after the layer/coating is deposited.

The reviewed literature on residual stress reveals that managing stress is important for maintaining the mechanical properties of the deposited layers. Uncontrolled residual stresses can lead to issues such as cracking, warping, and overall deterioration of the part's performance. Various methods, including preheating, clamping, adjusting energy input, and altering deposition strategies, have been suggested to mitigate these stresses, but the literature does not yet provide a comprehensive solution that is both effective and economically feasible in industrial settings [3]. Existing studies focus on using general strategies, including preheating**,** post-weld heat treatment and adjusting energy input, to reduce stress, but the effect of specific deposition pattern, clamping methods along energy input parameters in GMAW-WAAM processes have not been fully explored, which can help better design the setup for practical applications

As this research project is a sub-project, which belongs to the development of fully automated regeneration, repair and hardfacing techniques using automatic toolpath generation based on 3D vision control and monitoring. The goal of the research is not only to expand the knowledge of residual stress in WAAM processes, but also to offer practical solutions that can improve the reliability and performance of WAAM-deposited Stellite 6 layers in industrial applications. The current thesis is therefore aims to make the first attempt to i) optimizing the Stellite 6 deposition at low heat input using a GMAW based WAAM system, which includes a Miller weld heat source, a 3D camera and a robotic arm; ii) have a better understanding of the residual stress development during Stellite 6 hardfacing when using a zigzag deposition pattern. These research results can lay foundations for the further development of the automated deposition using WAAM. In addition, the residual stress measurement can help the refinement of the automatic toolpath generation algorithm and hardware setup design. This work will contribute to establishing WAAM as a reliable and efficient technology for high-value component repair, hardfacing and fabrication. Considering the above mentioned, the following research questions have been formulated to guide the investigation:

1. How can the deposition of Stellite 6 using GMAW-based WAAM be optimized to minimize residual stress and deformation?
2. What are the effects of different clamping configurations and specific deposition strategy on the development and distribution of residual stress in WAAM-deposited Stellite 6 layers?

3. Experimental setup, materials and methods

This chapter described the experimental framework used in this thesis, including the materials, the setup, and the methodologies. The aim is to have a thorough explanation of the procedures and equipment employed to ensure the reproducibility and validity of the experimental results.

3.1. Experimental setup

In this study, all printing tests were conducted at RAMLAB BV using a Cobot Techman^{TM12} robot with an 800 mm × 400 mm × 300 mm build volume integrated with a welding source named as the Miller Auto-Continuum^{TM} 350 together with a MaxQ repair software suite. Figure 13 shows the actual setup that was used during experiments.

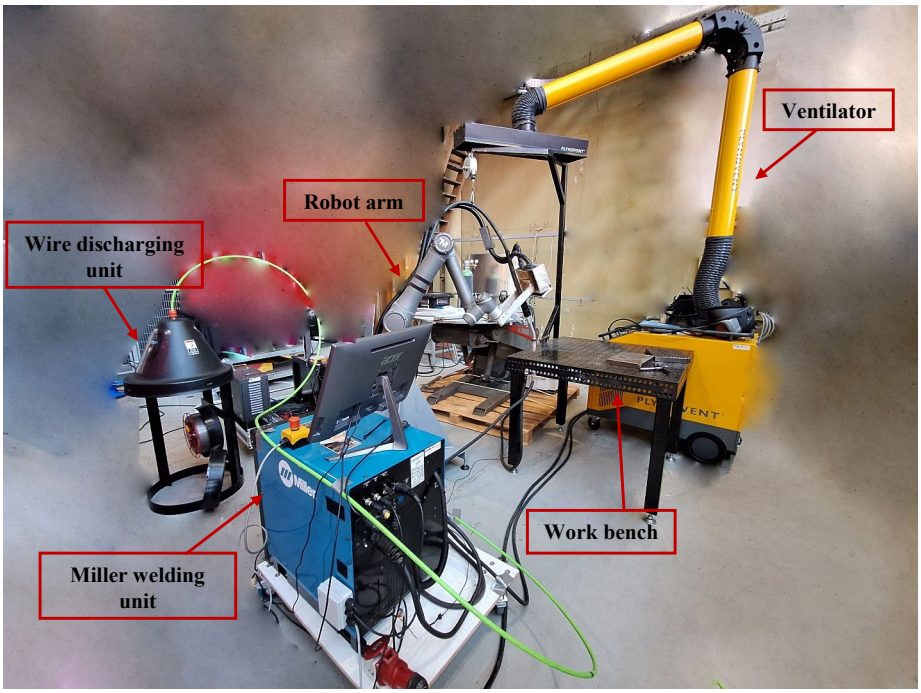

Figure 13. Actual experimental setup used for tests.

The software utilized for designing the deposition tool path was Autodesk PowerMill (Autodesk B.V, Hoofddorp, Netherlands) and MaxQ software suite (RAMLAB B.V., Rotterdam, Netherlands). Figure 14 illustrates the planned experimental setup for the Stellite 6 deposition path to fabricate specimens for residual stress measurement. The deposition process of Stellite 6 was carried out continuously, with no intermediate cooling between the deposition of adjacent layers. Moreover, the torch was consistently positioned perpendicular to the workpiece (PA position).

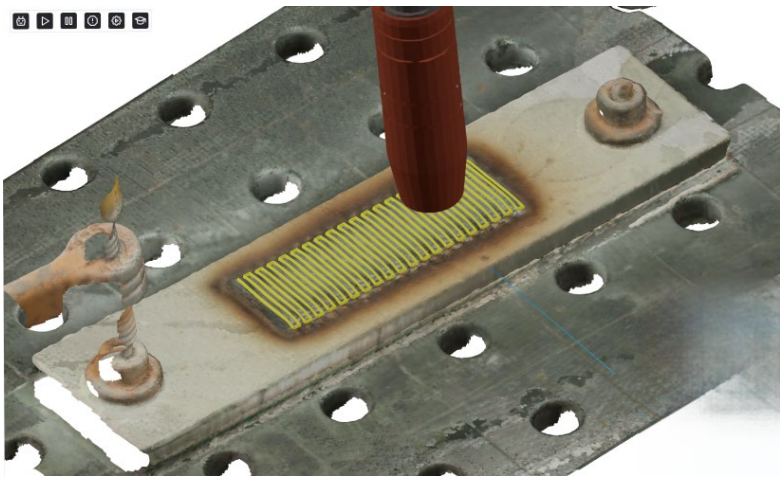

Figure 14. Stellite 6 deposition process captured and planned toolpath using the MaxQ 3D visualization functions.

3.2. Materials used in the Experiments

In this study, an AISI 316L stainless steel base plate measuring 250 × 60 × 10 mm^3 was used. Stellite 6 metal-cored wire with a diameter of 1.2 mm as the filler material, provided by industrial partner under a non-disclosure agreement (NDA). The chemical composition of the materials utilized in this study is presented in Tables 1 and 2. Inomaxx®2 was employed as the shielding gas for the Stellite 6 deposition, with its chemical composition detailed in Table 3. The shielding gas was supplied by Air products. The shielding gas flow rate was consistently maintained at approximately 20 l/min across all depositions. Prior to the deposition process, the base plate was cleaned using ethanol (99.9%, CH_3CH_2OH).

Table 1. Chemical composition of AISI 316L stainless steel, Fe balance.

Element	***C***	***Mn***	***Si***	***Cr***	***P***	***S***	***Mo***	***Ni***	***N***
[wt.%]	0.030	2.00	0.75	18.00	0.045	0.030	3.00	14.00	0.10

Table 2. Chemical composition of Stellite 6, Co balance.

Element	***C***	***Mn***	***Si***	***Cr***	***Fe***	***Mo***	***Ni***	***W***
[wt.%]	1.22	0.26	1.22	29.5	1.72	0.08	2.29	4.6

Table 3. Gas used in this study

Name	***Composition***	***Depositing Material***
INOMAXX®2	2% CO_2 in Argon	Stellite 6

3.3. Experimental Methods

The Miller Auto-Continuum™ 350 system offers a range of welding programs (welding modes), each specifically designed to optimize performance for particular wire and shielding gas combinations. In the process of optimizing the welding parameters for this study, two welding modes were investigated: Accu-Pulse® and Versa-Pulse™. The Accu-Pulse® welding mode is a versatile welding mode suitable for a wide range of industrial applications, offering an adaptive arc that is well-suited for materials ranging from 16 gauge (1.6 mm) and thicker according to [39]. The Versa-Pulse™ welding mode is particularly well-suited for high-speed automation on materials with a thickness of 1/4 inch (6.35 mm) or less, offering benefits such as low heat input, minimal spatter, and superior gap-filling capabilities [39].

3.3.1. Bead Shape and Process Stability Evaluation

To achieve optimal process parameters, characterized by a defect-free output and minimal heat input, good bead shape with sufficient hardness, the coldest deposition mode was prioritized. These conditions were considered critical, as the Miller welding system does not inherently provide a direct CMT setting. Subsequently, a series of experimental trials were designed and conducted, categorized as follows:

a) Single Beads: In this set of experiments, a single bead was deposited with consistent process parameters maintained along its entire length.

b) Overlap Beads: In these trials, overlapping beads were applied, with each bead covering 45% of the width of the previously deposited bead. Both single and overlapped beads were deposited to a length of 12.6 cm.

Following the deposition, the samples underwent standard metallurgical preparation, which included cutting, mounting, grinding, and polishing. The cross-sections of the prepared samples were subsequently etched using Kalling's No. 1 etchant to reveal microstructural characteristics. Microstructural observations were performed using optical microscopy with a Keyence VHX-2000 Digital Microscope (Keyence, Osaka, Japan).

a) Single Bead Deposition using Miller System

An investigation was conducted to determine the welding parameters for single bead deposition while minimizing the input heat using the miller system. As optimal process conditions (heat input between 0.1 – 0.2 kJ/mm) was obtained based on previous work reported by Lin [19] at RAMLAB. The conditions were adapted to the miller system used in this thesis and tested. For the bead shape and hardness evaluation, single bead and overlapping bead deposition can be performed on the normal steel substrate. Then this condition can be applied on the stainless substrate or other types of steel substrate with minor modification when using the low heat input process condition [19]. This maybe attribute to that with low heat input, there will be less dilution that not jeopardizing the integrity of the properties of the coating material. In this case, six single bead with heat input within the optimal heat input range mentioned earlier were deposited using Stellite 6. These tests, as shown in figure 15, used variations in the deposition parameters which are shown in table 4. For this series of tests, the Accu-Pulse® welding mode was tested. Considering the heat input, resulting bead shape, bead appearance

and process stability, the test number 6 was identified as the candidate for further overlapping tests and then sample preparation for the hardness measurements.

Figure 15. single bead deposition of Stellite 6 with Accu-Pulse® welding mode

Table 4. single bead deposition parameters of Stellite 6 with Accu-Pulse® welding mode

Tests numbers	*Arc Length (Miller system)*	*Wire Feed Speed [m/min]*	*Arc Control*	*Actuals*		*Travel speed [m/min]*	*Heat input [kJ/mm]*
				U [V]	*I [A]*		
1	80	4.98	25	21.08	128	0.3	0.539
2	80	3	25	19.43	78	0.3	0.303
3	60	5	25	26.17	124	0.45	0.346
4	65	4	25	18.60	100	0.70	0.127
5	70	4	25	23.87	125	0.65	0.220
6	70	4	25	23.97	119	0.65	0.210

b) Overlapping Beads using Parallel Beads

The Stellite 6 was intended to be the hardfacing material on the stainless steel. To adapt the process condition on the stainless steel on the pre-deposited stainless steel 316L layers, a Stellite 6 bead was testing deposited on this pre-deposited austenitic stainless steel surface. After measuring the width of the initial bead (7.3 mm), four additional overlapped beads were deposited adjacent to the first. For each subsequent deposition, the robot arm was laterally displaced by 55% of the bead's width (4.015 mm) to ensure proper overlap, as depicted in figure 16. In figure 16, the red circles highlight areas where issues, suspected to be related to wire feeding, were observed. These are typical indication that additional heat input is need for having full melting at the weld toe. This may be already addressed with the zigzag deposition as that it had been reported [3] that causes of inter-run-porosities can be addressed when there is sufficient heat input and maintaining the cold process conditions.

Figure 16. overlap beads deposition of Stellite 6 on top of stainless steel overlapped beads.

i) Cross Section of the Deposited Layers Using Straight Line Strategy

Deposit shown in figure 17 was cut at the centre to extract samples for further metallurgical analysis. After undergoing standard metallurgical preparation, the cross-sectional area of the sample before and after etching is shown in figure 17. The interface between the stainless steel deposits and the base plate reveals discernible porosities, visible even to the naked eye. These are typical inter-run-porosities. A rough estimation is that the dilution between the stainless steel layer and Stellite 6 layer is more than 30%. This high level of dilution suggests that further optimization is required, specifically aimed at reducing the heat input during Stellite 6 deposition.

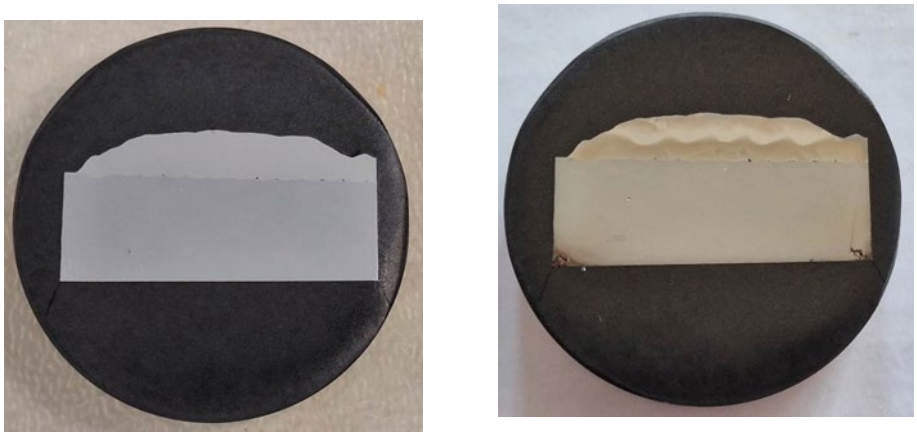

(a) (b)

Figure 17. The cross section of the sample (a) before and (b) after etching.

Figure 18 shows a more detailed micrograph of sample. There is no crack observed for both stainless steel and Stellite 6 layers. Inter-run-porosities mostly happened at the weld toe regions between adjacent beads of the stainless steel layer. For the Stellite 6 layer, it appears to be good except for a pore noticed at the bottom of the fourth bead, which could be caused due to impurities or oxides remaining on the deposited stainless steel surface.

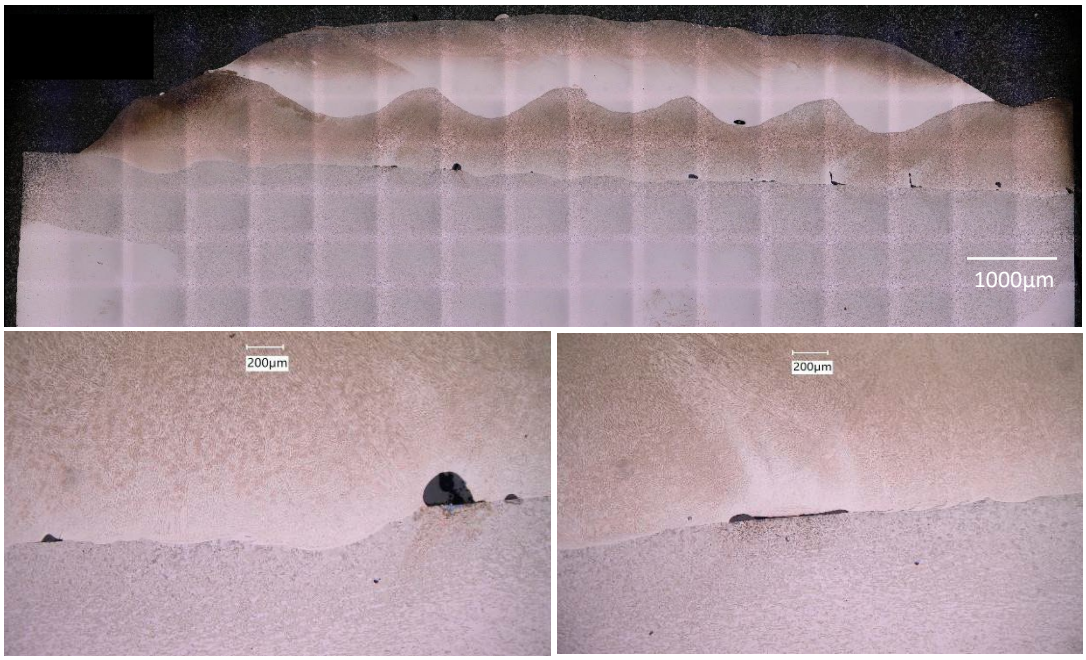

Figure 18. Micrographs captured utilizing the Keyence VHX-2000 Digital Microscope from Osaka, Japan.

The Vickers microhardness (HV 0.5, with 0.5 kgf) was measured across the cross section of the sample. Figure 19 shows the measured hardness along the vertical direction of the deposited layers. The average measured hardness of Stellite 6 deposits was 372.87 HV. The typical hardness of Stellite 6 is between 380-490 HV. The reduction of the Stellite 6 is due to the excessive Fe dilution from stainless steel layer, which can lead to hardness reduction [3].

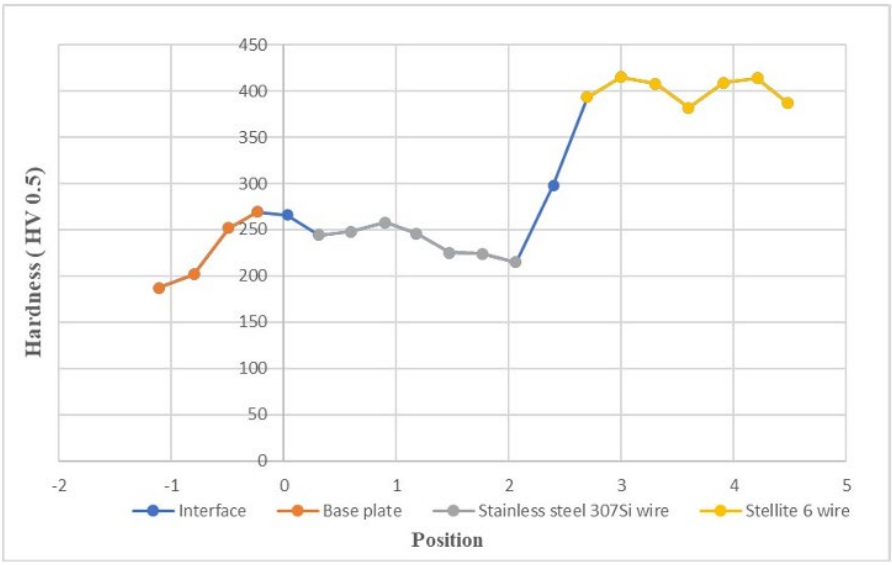

Figure 19. Hardness measured of the deposited layers using a Struers DuraScan-70 hardness tester from Struers Inc. in Westlake, USA.

c) Heat Input Further Optimisation using the Versa-Pulse™ Mode

To further reduce the heat input and following the suggested Miller system settings, a few trails were made using Versa-Pulse™ welder. Six single bead tests were conducted utilizing the Versa-Pulse™ welding mode which are even colder settings that can lead to a more substantial reduction of the input heat. However, spatter and process instability were noticed, as shown in figure 20. The test conditions are provided in table 5. Based on the evaluation the tests as shown in figure 20, further optimize the process stability to reduce spatter and improving bead uniformity.

Figure 20. single bead deposition of Stellite 6 with Versa-Pulse™.

Table 5. single bead deposition parameters of Stellite 6 with and Versa-Pulse™.

Tests numbers	*Arc Length (Miller system)*	*Wire Feed Speed [m/min]*	*Arc Control*	*Actuals*		*Travel speed [m/min]*	*Heat input [kJ/mm]*
				U [V]	*I [A]*		
1	70	4	25	19.1	97	0.75	0.119
2	70	4	25	19.5	98	0.70	0.131
3	70	4	25	19.3	99	0.65	0.141
4	70	4	25	19.2	96	0.60	0.147
5	70	3	25	18.7	75	0.65	0.103
6	75	4	25	19.5	95	0.65	0.136

d) Overlapping Beads using Zigzag Strategy

The oscillation strategy was selected for further testing, in contrast to the previously used straight line deposition. As the oscillation will maintain the arc on during the layer deposition process, it can preheat the substrate to encourage the melt pool spreading better. Effectively, the oscillation increases the substrate temperature as the arc is continuously turned on, which can help to improve the material's wettability. This can overcome the narrow bead shape due to cold process conditions. It is therefore expected to also solve the issues of inter-run-porosity formation as shown in the earlier section. The corresponding design toolpath for oscillation is schematically shown in figure 21. A new layer of Stellite 6, as shown in figure 22, was deposited on the pre-deposited stainless steel surface using an oscillating deposition toolpath, following the parameters outlined in test condition 1 from table 5.

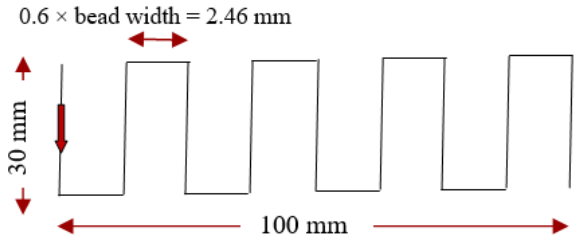

Figure 21. A schematic drawing of the oscillating welding path.

Figure 22. Overlap beads deposition of Stellite 6 on top of stainless steel deposits with oscillating depositing path

i) Cross Section of the Deposited Layers Using Oscillation Strategy

The deposit shown in figure 22 was cut at centre along and perpendicular to the deposition directions. Samples were extracted for further metallurgical analysis. The cross section of the sample before and after etching are depicted in figure 23. The overview observations show that the deposit is free from visible defects and fully dense layers were deposited. Figure 24 shown micrographs of the cross sections. It shows that defect free deposited layer was obtained with this condition.

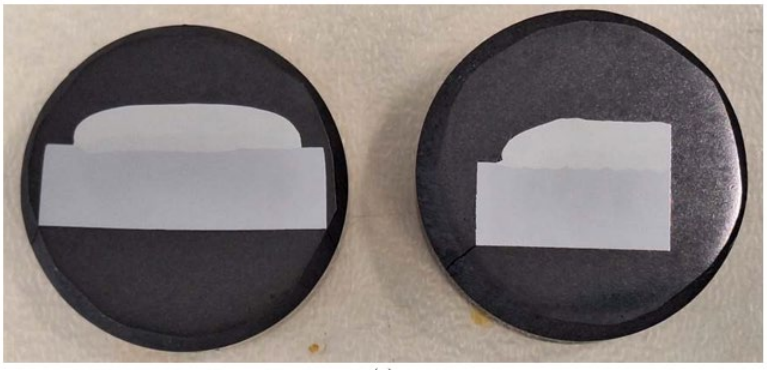

(a)

(b)

Figure 23. The cross section of the sample (a) before and (b) after etching; Left side is cut along weld direction and perpendicular to deposition direction; Right side is cut perpendicular to weld direction and along the deposition direction.

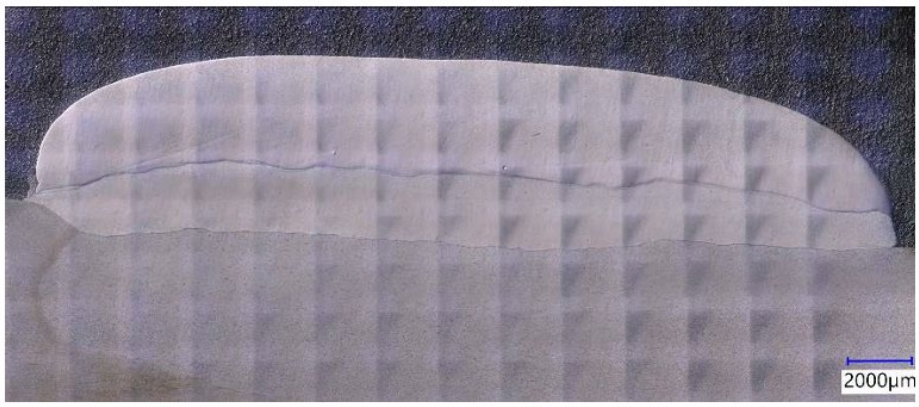

(a)

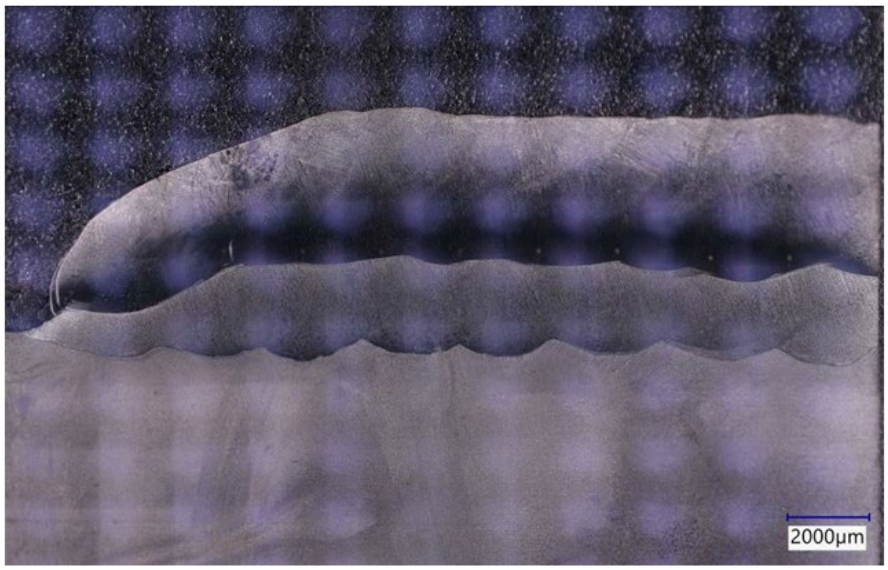

(b)

Figure 24. Micrographs captured utilizing the Keyence VHX-2000 Digital Microscope from Osaka, Japan. (a) transverse section image of the sample, (b) Longitudinal section image of the sample.

The Vickers microhardness (HV 0.5, using a 0.5 kgf load) was measured along the deposited layers for both transverse and the longitudinal cross sections. Figure 25 shows the variation in hardness along the vertical direction of the deposited layers. The average measured hardness for Stellite 6 deposits was 347.83 HV.

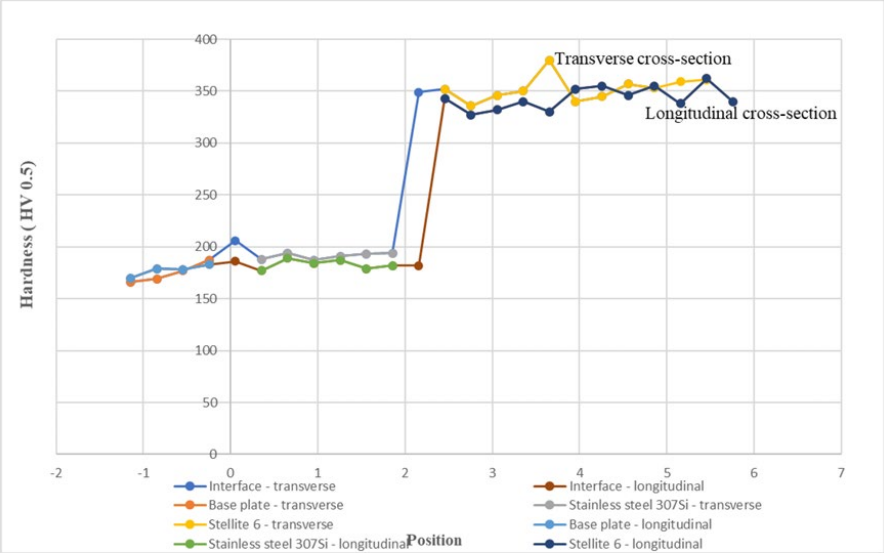

Figure 25. Hardness measured of the deposited layers for both transverse and the longitudinal cross sections using a Struers DuraScan-70 hardness tester from Struers Inc. in Westlake, USA.

An optimal condition when using the zigzag (oscillation) pattern as shown in figure 26 (dimensions of 25 mm × 50 mm), was found with setting including an arc length of 65, distance from end of wire electrode to workpiece [40], a wire feed speed of 4.5 m/min, and a travel speed of 0.85 m/min, resulting in a heat input of 0.163 kJ/mm. A uniform overlapping layer thickness of approximately 2.0 mm was obtained with spatter reduced.

Figure 26. oscillation pattern deposited with optimal process parameters.

3.3.2. *Experiment Design for Evaluating the Residual Stress Built up*

The experimental design focused on investigating the effects of releasing temporary fixtures, specifically to evaluate the differences in residual stress levels before and after the removal of clamps. Residual stress measurements will be conducted using the hole drilling method, with the contour method employed as a complementary technique to validate and cross-reference the results obtained from hole drilling.

Two distinct deposition configurations were analysed in this study. In the first configuration, a sample featuring an oscillation (zigzag) pattern was deposited at the centre of the base plate, with the workpiece secured by two clamps. In the second configuration, only one side of the base plate was clamped to the worktable, leaving the opposite side unsupported. Figure 27 schematically shows the arrangement of clamps and the base plate for both test configurations.

Each clamping method was tested under two different deposition conditions: one involving a single layer of deposition, and the other involving two layers. A total of four samples were fabricated, as outlined in table 6, which summarizes the number of deposition layers and the corresponding clamping methods for each sample. This experimental design facilitates the examination of both the influence of clamping and the number of deposition layers on the development of residual stress. Specifically, for samples with the same clamping configuration, the effect of varying the number of layers is assessed. Then, for samples with a constant number of layers, the influence of different clamping methods is evaluated.

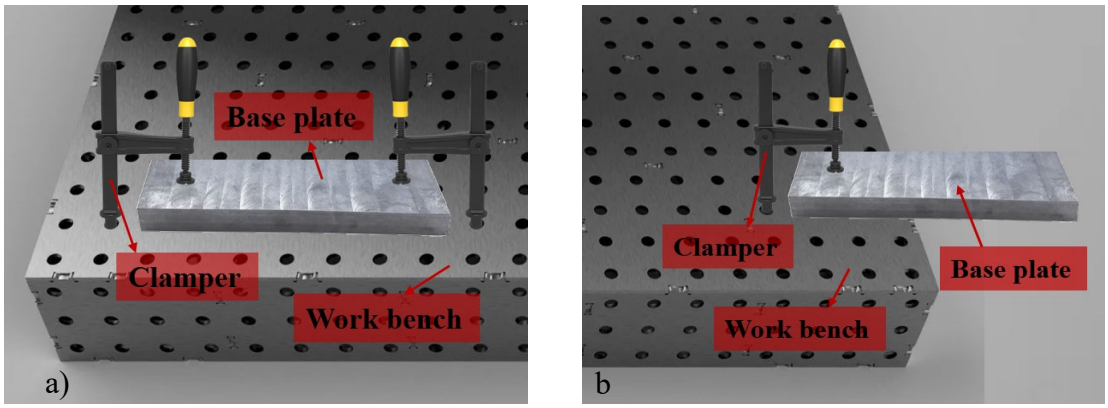

Figure 27. Schematic representation of the clampers and base plate placement for a) the first configuration and b) the second configuration.

Table 6. Summary of number of layers and clamping method for each sample

Sample number	*Type of Configuration*	*Number of layers*
1	First	1 layer
2	First	2 layers
3	Second	1 layer
4	Second	2 layers

3.4. *Depositing Samples for Residual Stress Measurements*

Using GMAW with the optimized process parameters identified in Section 3.3.1, specifically part d-i, samples were made for residual stress analysis. In appendix A, figure 39 presents the side (a) and top (b) views of sample 1 before unclamping. Similarly, figures 40-42 show the side (a) and top (b) views of sample 2, sample 3, and sample 4 before unclamping, respectively. In appendix B, figure 43 shows the side (a) and top (b) views of sample 1 after unclamping, followed by figures 44-46, which display the identical views for samples 2, 3, and 4. Additionally, figure 47 (appendix B) provides a comparative visual of all samples side by side, both from the top (a) and side (b) views, highlighting any visible differences after unclamping. As shown in figure 47 (appendix B), samples 2 and 4, which consist of two layers of Stellite 6, exhibited increased spatter during the deposition process. This increase in spatter is likely due to the continuous nature of the deposition, where no intermediate cooling or surface cleaning occurred between adjacent layers. The lack of cleaning can lead to surface contamination, such as the formation of oxides, slag, or other impurities on the first layer. These contaminants may cause increased spatter when the second layer is deposited.

To determine whether beam stress results in compression or tension within the section's fibres, the curvature of the beam's deformation is a critical factor. When the beam bends into a sagging "U" shape, the top fibres experience compression (negative stress), while the bottom fibres are subjected to tension (positive stress) [41]. As shown in figures 43-46 (appendix B), all fabricated samples exhibit a sagging "U" shape, indicating that the stress distribution follows a pattern similar to that shown in figure 28.

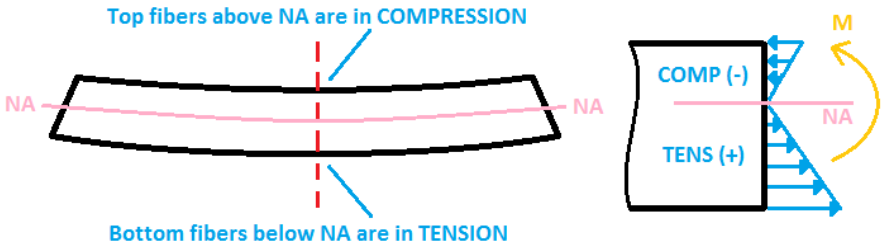

Figure 28. Stress Distribution in a Sagging "U" shape Beam [41]

The vertical deflection (displacement) and Stellite 6 layer thickness for all samples were measured using a calliper after unclamping. The results are presented in table 7.

Table 7. Vertical deflection and Stellite 6 layer thickness measured after removing the clamps on a flat table.

Sample Number	*Vertical Deflection (Displacement) [mm]*		*Stellite 6 layer thickness [mm]*
	Left Side	**Right Side**	
1	2.15	3.3	2.1
2	3.1	1.25	4.15
3	8.05	6.2	2.05
4	9.35	10.3	4.3

3.5. *Sample Preparation for Residual Stress Measurement using Hole Drilling Method*

To prepare the samples for residual stress measurement, each sample's surface was initially light ground to create a relatively smooth surface, though some lines between the passes of GMAW were still visible. Further fine light grinding was carried out to improve surface smoothness. Afterward, the sample faces were degreased by applying a caustic solution, which was subsequently neutralized to enhance strain gauge adhesion. The rosette strain gauges were then carefully positioned at the centre of each sample, with particular attention given to maintaining a significant gap between any visible GMAW pass lines and the area directly under or between the rosette's gauges.

The strain gauges were fixed to the prepared surfaces using cyanoacrylate glue. Before beginning the drilling process, the rosettes attached to the specimens were connected to a Micro-Measurements P3 Strain Indicator and Recorder (P3), which was responsible for capturing and converting the strain gauge readings into microstrain values, then transferring them to a computer for further analysis [42]. The gauges in each rosette were consistently numbered 1-3, corresponding to the P3 system. To ensure accurate strain measurements, the strain indicator was calibrated with the gauge factors for each of the three gauges, allowing proper scaling between current changes and strain. Each gauge was then balanced to provide an initial reading of zero. Figure 29 shows a sample with the strain gauge attached and the drill positioned over the central point.

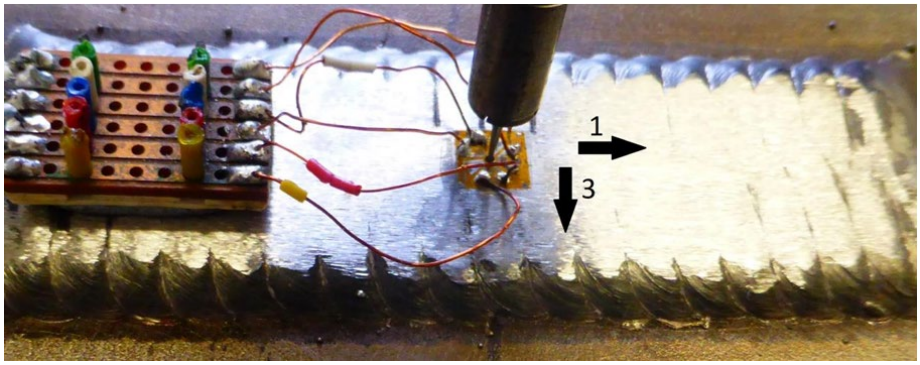

Figure 29. Sample with the rosette attached and drill in position, including indications of gauge orientations.

After the rosette strain gauges were installed and connected, each sample was securely mounted onto a flat, levelled table where the Stresscraft 3-axis drilling machine was fixed in place. Maintaining controlled environmental conditions was crucial; the room temperature was kept constant at 21°C, and the setup was shielded from direct sunlight, as fluctuations in either could cause a measurable strain response. To ensure the hole was drilled perpendicular to the concave surface, the samples were carefully aligned so that the target location was level with the measurement table, while minimizing the applied forces to prevent interference with the accuracy of the results. Once the sample was properly secured, the drill was precisely aligned with the centre of the rosette strain gauge.

The measurements were conducted using strain gauges designed for the specific thickness of the samples. Encapsulated rosettes with a gauge length of 0.785 mm (Micro Measurements EA-06-031RE-120) were used, which are suitable for hole diameters between 0.8 and 1.0 mm. These rosettes consist of three gauges oriented at 0°, 90°, and 225° (equivalent to 45°). Given concerns about drill wear, the 031 gauges were selected over the larger 062 gauges to reduce hole diameter and depth, thereby minimizing wear on the drill bits and ensuring the validity of the results.

For the drilling, inverted cone tungsten carbide burs with a diameter of 0.8 mm were employed. A fresh bur was used for each drilled hole to minimize friction and heat generation, which could otherwise affect the measurement. Each drilling operation was performed in increments, with a depth increase followed by a circular orbital motion to ensure the hole diameter remained within the limits set by the strain gauges. This method also helped to limit heat generation by reducing contact between the drill and the sample. Compressed air was used to remove debris before each measurement, ensuring a clean surface for accurate readings.

Before starting the actual drilling, a series of incremental drill passes was performed to establish the zero-depth reference point. This was achieved by drilling progressively through the centre of the strain gauge until the dot marking the target location was removed, indicating that the drill had just begun to penetrate the sample material. To ensure the most accurate determination of the zero-depth reference, both the bottom surface of the hole and the drilling debris were closely monitored using a magnifying lens, as the appearance of both noticeably changes once the sample material is reached.

Once the zero-depth reference was identified, the drill's coordinate system was reset to zero, as were the microstrain values on the P3 Strain Indicator. After defining the zero-depth reference, the pre-programmed drilling process commenced, with a series of incremental drills proceeding from the top surface of the sample. After each increment, the system was allowed to stabilize before recording the results, and then the next increment was drilled. These strain measurements were then used to calculate the relieved stresses.

Upon completing the drilling process, the sample was carefully removed from the measurement table, and the dimensions of the drilled hole were precisely measured using an optical microscope. Both the depth and the diameters at the surface and bottom of the hole were recorded. Using the sample's elastic properties, the relaxed strain values at each predefined depth, and the measured hole diameter, the in-plane stress profile along the hole depth was back-calculated using the integral method, which is explained in more detail in chapter 4 section 4.2.

A total of four ICHD measurements were carried out following the detailed experimental procedure. One exception occurred in Sample 4, where an error resulted in the initial hole being drilled without recording data. As a result, the measurement was taken along the midline of each pass, but the nearest point to the original hole was approximately 12 mm away.

4. Results and Discussion

This chapter 4 presents the results and discussion of the research. This chapter begins with a detailed analysis of deformation behaviour FEA to simulate the thermal and mechanical behaviour of the material during GMAW process. It then moves into the core of the study, which is the investigation of residual stress distribution in printed parts, particularly using the Incremental Central Hole Drilling method. The chapter evaluates the effects of process parameters, including the number of deposition layers and clamping configurations, on the residual stress profile.

4.1. Finite Element Analysis on the Deformation Induced during the Sample Deposition

Finite Element Analysis (FEA) is a commonly applied numerical method for estimating solutions to boundary value problems involving partial differential equations [33]. In this study, a FEM was built using COMSOL Multiphysics (version 6.2) to simulate the residual stresses and deformation induced during the sample deposition. The model aimed to capture the thermal and mechanical behaviour of the sample during and after the deposition, which involved transient heat transfer and the consequent thermal expansion, leading to residual stresses and bending.

The geometry was created in a 3D, where two domains represented the SS316L steel substrate and the deposited Stellite 6 layer. Circular cutouts on both ends of the substrate represented the locations of clamps used to secure sample 1 and 2 during the deposition process, while for sample 3 and 4, a single circular cutout on one end was used. A union operation was performed to ensure continuity between the blocks. Two materials from COMSOL's material database were assigned to different domains. The materials were defined with temperature-dependent properties to account for the variations at elevated temperature during the deposition process. The thermal and mechanical properties, such as young's modulus, poisson's ratio, and thermal expansion coefficients, were specified for both materials, when assigning the material to the domain. The solid mechanics physics interface was used to capture the structural behaviour of the samples. Two separate material models were defined under this interface, Linear Elastic Material 1 for the substrate and Linear Elastic Material 2 for the deposited layer. These models incorporated the isotropic material properties of both materials. To account for thermal effects during the deposition process, thermal expansion was included in the solid mechanics module. This feature captured the thermal strains resulting from the temperature gradient between the maximum temperature (1683.2 K, which is the liquidus temperature for Stellite 6) and the room temperature. The thermal expansion coefficients for the materials were set accordingly, with a reference temperature of 298.15 K.

The boundary conditions were defined to simulate the clamping constraints and the initial conditions of the model. Fixed constraints were applied to the circular cutouts at the ends of the substrate to simulate the clamps holding the samples in place during the deposition process, preventing displacement and rotation at these points. The initial values for displacement and velocity were set to zero across all domains, representing the undeformed state of the sample at the beginning of the simulation. The model utilized a fine tetrahedral mesh, particularly refined meshed were used in the region around the deposited layer.

The behaviour of the system is governed by the following equations, which are specified in the equation section under the settings tab of the corresponding physics interface in COMSOL:

- Mechanical equilibrium equation (balance of forces):

$$\nabla \cdot (FS^T) + F_V = 0 \quad (4),$$

where F is the deformation gradient tensor, S is the second Piola-Kirchhoff stress tensor, and F_V represents the volume force.

- Strain tensor:

$$\varepsilon = \frac{1}{2}(\nabla u + (\nabla u)^T + (\nabla u)^T \nabla u) \quad (5),$$

where u is the displacement field.

- Thermal expansion strain:

These equations were used to simulate the transient heat transfer and the resulting thermal and structural deformations during the sample deposition process.

$$\varepsilon_{th} = \alpha(T) \cdot (T - T_{ref}) \quad (6),$$

where, $\alpha(T)$ is the temperature dependent coefficient of thermal expansion, T is the temperature and $T_{ref}$is the reference temperature.

Because linear elastic materials are being used for both the substrate and the deposited layer, the stress-strain relationship in this context is governed by Hooke's Law for isotropic materials:

$$S = C(E, \nu) \cdot \varepsilon \quad (7)$$

where $C(E, \nu)$ is the material stiffness matrix dependent on the young's modulus E and poisson's ratio ν. These equations capture the fundamental physical behaviour of the system, including the mechanical deformations, stress distributions, and thermal effects induced by the sample deposition process.

Two studies were conducted to capture both the transient and steady-state behaviour of the system. The first, a stationary study, focused on capturing the steady-state thermal and mechanical response of the samples. Geometric nonlinearity was enabled in this study to account for large deformations induced by thermal expansion and residual stresses. The solver configuration used a stationary solver to compute the equilibrium state of the system, with an emphasis on the von Mises stress distribution and displacement fields. The second study was time-dependent and designed to simulate the dynamic thermal and structural response during the welding process. The time unit was set to microseconds, and the output times were specified within a range of 0 to 100 µs. The solver for this study captured the transient heat transfer and the resulting structural deformations during both the heating and cooling phases. A fine time-stepping (0.1 µs) was employed to ensure accurate temporal resolution of the

thermal effects and associated stresses. For both studies, solver configurations were set to automatically choose appropriate methods for solving the solid mechanics equations. The stationary solver included geometric nonlinearity to capture the nonlinear relationship between stress and strain under large deformation conditions. The time-dependent solver, on the other hand, utilized interpolation-based output to capture results at specific time intervals. Figures 30-33 show the displacement magnitude for samples 1 through 4, respectively, after complete cooling down to room temperature. The key results of this modelling process focused on the von Mises stress distribution and the displacement of the welded sample after the welding process. The displacement values measured after unclamping the samples were previously reported in table 7. Samples' displacement differs between the clamped state on the welding table and after being unclamped. To account for this, the displacement of the samples while clamped to the welding table was also measured using side-angle photos taken immediately after welding, with online tool [43] used to verify the results. These measurements were consistent with the simulation results. While the displacement values aligned well with experimental observations, the simulated von Mises stress values were reported in the range of GPa. As the ultimate tensile strength of Stellite 6 is 1265 MPa, these stress values appear unrealistic. Although it is interesting to identify the reason or causes of why the model fail to provide reasonable residual stress level, it could not be completed within the timeframe of this master thesis project. But it is definitely worth further investigation and further development of current modelling approach, as it gives fairly good deformation that matched with the experimental observations, e.g., bending direction and deflection levels. To obtain the residual stress levels, the hole drilling method was employed and described in the next sections.

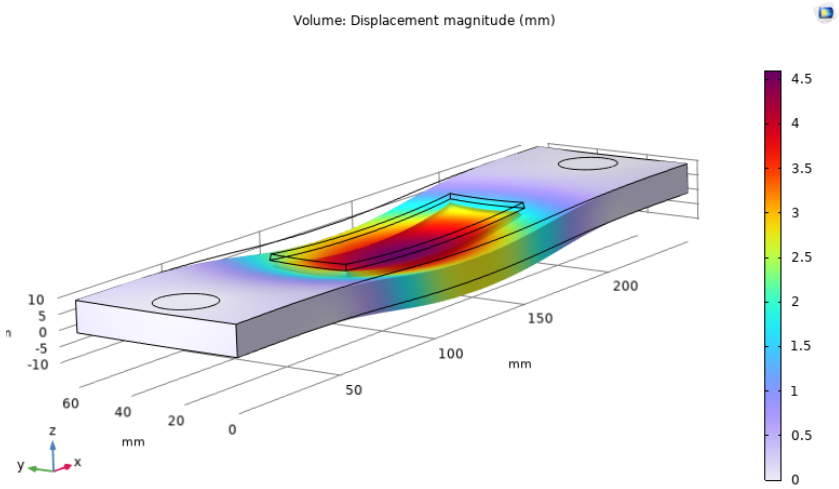

Figure 30. Displacement magnitude of sample 1 (mm)

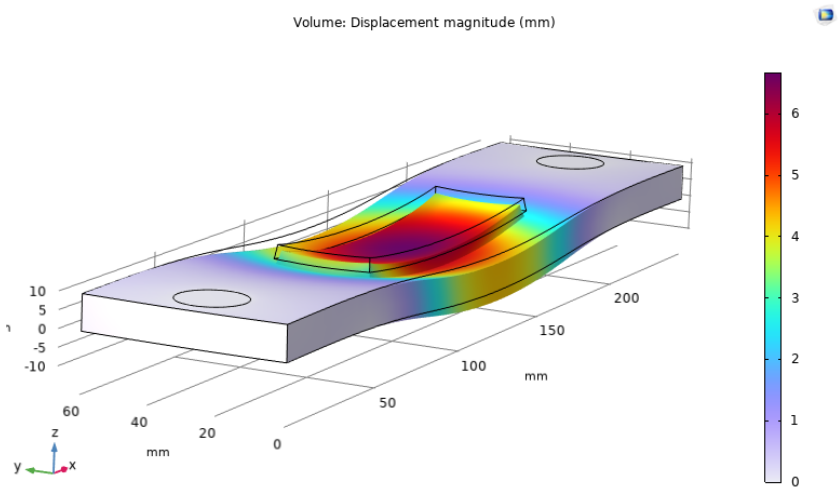

Figure 31. Displacement magnitude of sample 2 (mm)

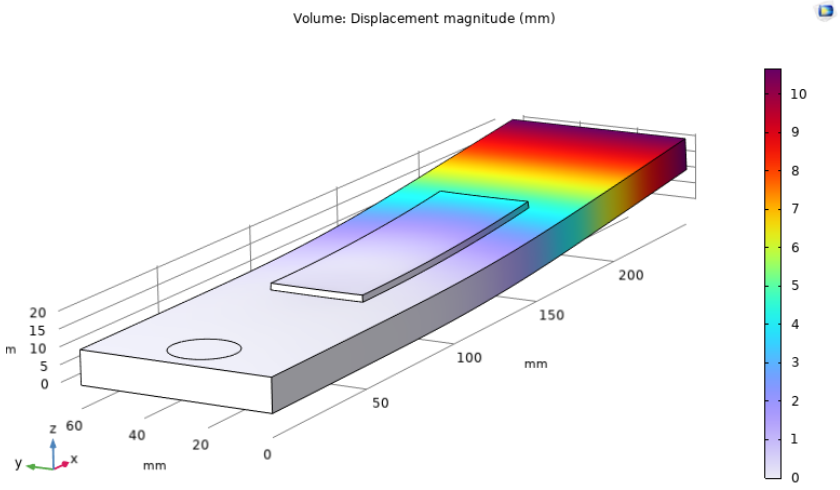

Figure 32. Displacement magnitude of sample 3 (mm)

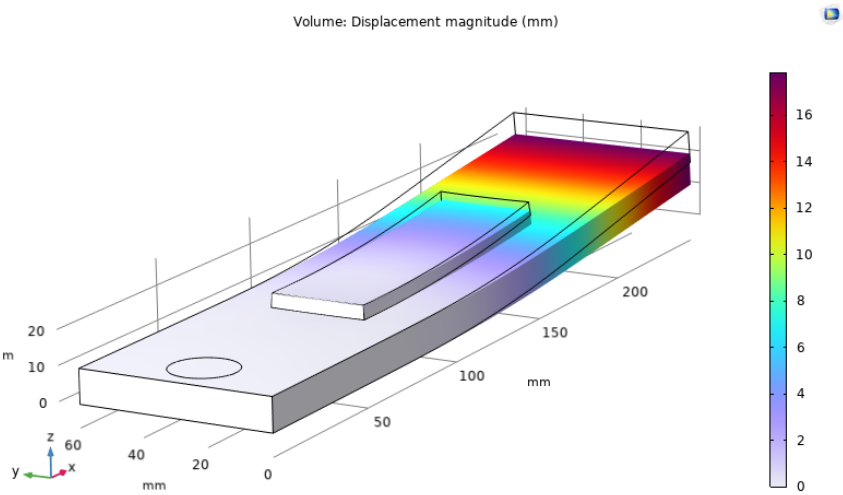

Figure 33. Displacement magnitude of sample 4 (mm)

4.2. *Incremental Central Hold Drilling Method (ICHD)*

The integral method for calculating non-uniform residual stresses from measured strain relaxations in the ICHD technique involves a systematic approach based on integral equations, transformed variables, and calibration coefficients. The stress components in a plane parallel to the specimen surface are represented by transformed stress variables for simplicity. Let $\sigma_1(H)$, $\sigma_3(H)$, and $\tau_{13}(H)$ represent the cartesian stress components at a depth H below the surface. The transformed stress variables are defined as [44]:

$$P(H) = (\sigma_3(H) + \sigma_1(H))/2 \tag{8}$$

$$Q(H) = (\sigma_3(H) - \sigma_1(H))/2 \tag{9}$$

$$T(H) = \tau_{13}(H) \tag{10}$$

Similarly, the strain relaxations $\varepsilon_1(h)$, $\varepsilon_2(h)$, and $\varepsilon_3(h)$ measured at depth h after drilling a hole are transformed as [44]:

$$p(h) = (\varepsilon_3(h) + \varepsilon_1(h))/2 \tag{11}$$

$$q(h) = (\varepsilon_3(h) - \varepsilon_1(h))/2 \tag{12}$$

$$t(h) = (\varepsilon_3(h) + \varepsilon_1(h) - 2\varepsilon_2)/2 \tag{13}$$

These transformed variables simplify the mathematical framework by decoupling the stress-strain equations, making the problem easier to analyse. The variables P and p conceptually represent the mean "pressure" of the residual stresses and the associated "volumetric" strain relaxations. The depth variables H and h are nondimensionalized in relation to the strain gauge's mean radius, r_m, as follows [44]:

H = Z/r_m = nondimensional depth from surface
h = z/r_m = nondimensional hole depth

where Z is depth from surface (in mm), z is hole depth (in mm) and r_m = 2.57mm for MM 062-RE gauge. The transformed strain relaxation $p(h)$ is measured after drilling a hole to a depth h. This strain represents the integral of the infinitesimal strain components resulting from the transformed stresses $P(H)$ at all depths within the range $0 \leq H \leq h$. This relationship is mathematically expressed as [44]:

$$p(h) = \frac{1+\nu}{E} \int_0^h \hat{A}\,(H,h)\, P(H)\, dH \qquad 0 \leq H \leq h \tag{14},$$

where $\hat{A}(H,h)$ represents the strain relaxation per unit depth caused by a unit stress at depth H, when the hole depth is h and ν is poisson's ratio. In practical situations, where strain relaxations are measured after increasing the hole depth in n discrete increments to depths h_i (with i = 1, 2, ..., n), it is useful to express this in a discrete form of the equation [44]:

$$\sum_{j=1}^{j=i} \bar{a}_{ij}\, P_j = \frac{E}{1+\vartheta}\, p_i \qquad 1 \leq j \leq i \leq n \tag{15},$$

where p_i is measured strain relaxation after the ith hole depth increment, P_j is equivalent uniform stress within the j'th hole depth increment, $\bar{a}_{ij}$ is strain relaxation due to a unit stress within increment j of a hole i increments deep and n is total number of hole depth increments. The relationship between the coefficients $\bar{a}_{ij}$ and the strain relaxation function $\hat{A}(H,h)$ is [44]:

$$\bar{a}_{ij} = \int_{H_{j-1}}^{H_j} \hat{A}\,(H, h_i)\; dH \tag{16}$$

In matrix notation, equation (14) and similar equations for the other two transformed stresses become [44]:

$$\bar{a}\,P = \frac{E}{1+\nu}\,p \tag{17}$$

$$\bar{b}\,Q = E\,q \tag{18}$$

$$\bar{b}\,T = E\,t \tag{19},$$

where the matrix $\bar{b}$ contains the coefficients corresponding to the cumulative strain relaxation function $\hat{B}(H,h)$, corresponding to the pure shear stress field, which is used to calculate the shear stress components at various depths during the hole drilling process. The cartesian stress components can then be recovered from the calculated transformed stresses using the following relationship [44]:

$$\sigma_1(H) = P(H) - Q(H) \tag{20}$$

$$\sigma_3(H) = P(H) + Q(H) \tag{21}$$

$$\tau_{13}(H) = T(H) \tag{22}$$

and the principal stresses are [44]:

$$\sigma_{max}(H), \sigma_{min}(H) = P(H) \pm \sqrt{Q^2(H) + T^2(H)} \tag{23}$$

$$\beta(H) = \frac{1}{2} tan^{-1}(\frac{T(H)}{Q(H)}) \tag{24}$$

where $\beta(H)$ is the angle measured clockwise from direction 3 to the maximum principal stress direction at depth H [44].

The calculated in-plane stresses include transverse stress (σ_1, aligned with each pass), longitudinal stress (σ_3, oriented along the start and end points of the GMAW toolpath), and shear stress (τ_{13}) components, relative to the final configuration of the samples. For clarity, the corresponding stress directions are shown in figure 34. For each sample, once the hole was measured, its size was used to calculate the corresponding stresses. Some variation in hole diameter was observed, with each hole being slightly smaller near the base. To account for this, the stress plots were generated based on an average of the hole diameters measured at the top and bottom. Error bars were included in the stress plots to reflect the uncertainty in the measurements. These were calculated using the minimum and

maximum hole sizes to show the potential variation in stress values. The obtained results present both the measured strains from the three strain gauges and the stresses calculated from these strain values, included in figures 35 to 38. The recorded microstrain measurements (a) and the corresponding calculated stresses (b) for Sample 1 are presented in figure 35. Similarly, the microstrain measurements (a) and calculated stresses (b) for Sample 2, Sample 3, and Sample 4 are shown in figures 36, 37 and 38, respectively. It is important to note that for each sample, the top few depths (up to 50 µm) may yield unreliable data due to stresses introduced during the grinding and/or polishing of the surface [45,46].

Figure 34. Schematic representation of in-plane stress components ($\boldsymbol{\sigma_1}$, $\boldsymbol{\sigma_3}$, τ_{13}) aligned with the GMAW toolpath

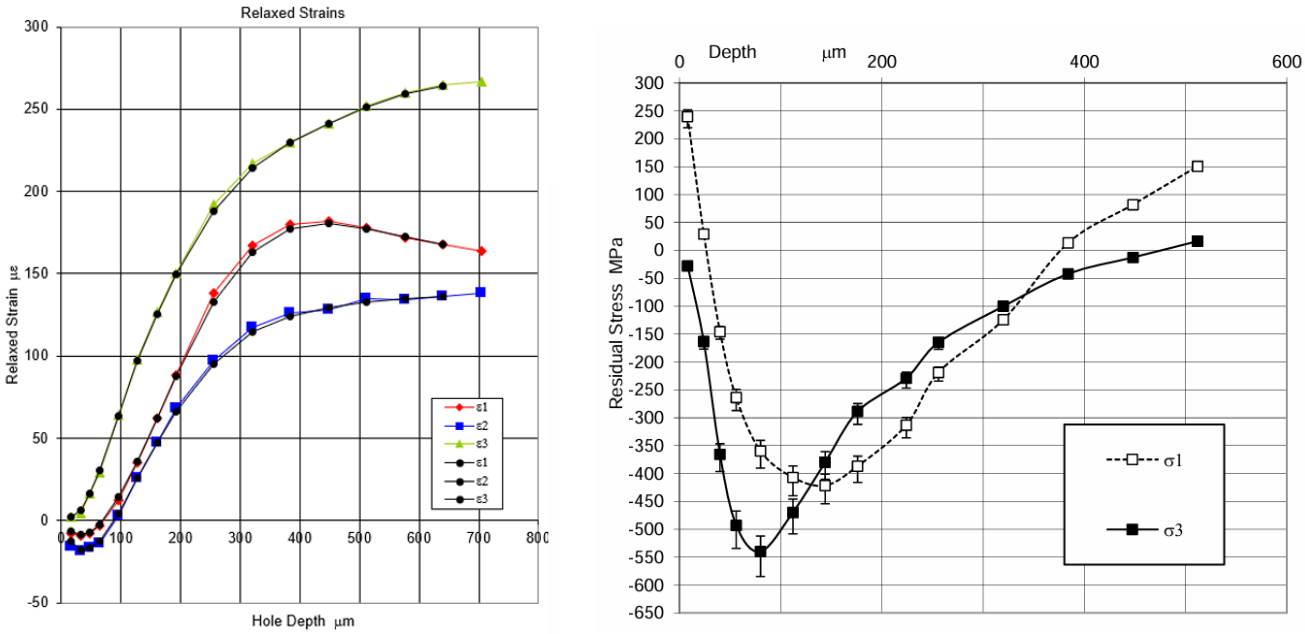

Figure 35. Recorded Microstrain Measurements (a) and Calculated Stresses (b) for Samples 1

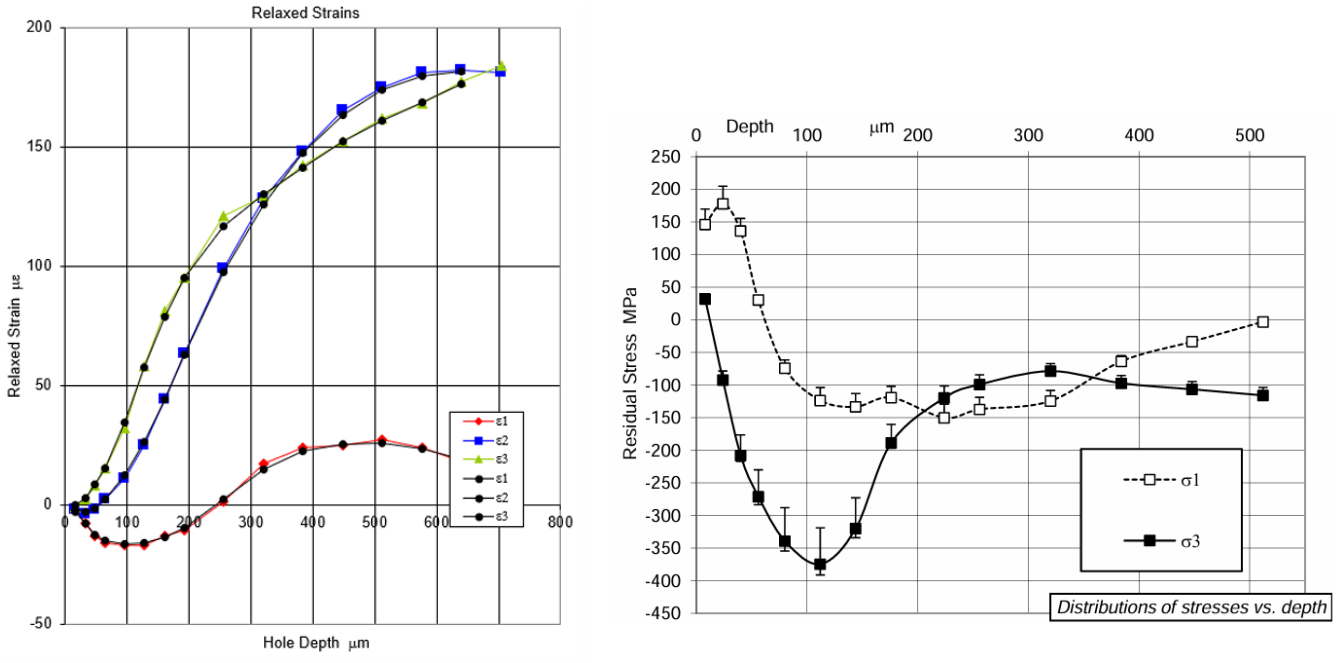

Figure 36. Recorded Microstrain Measurements (a) and Calculated Stresses (b) for Samples 2

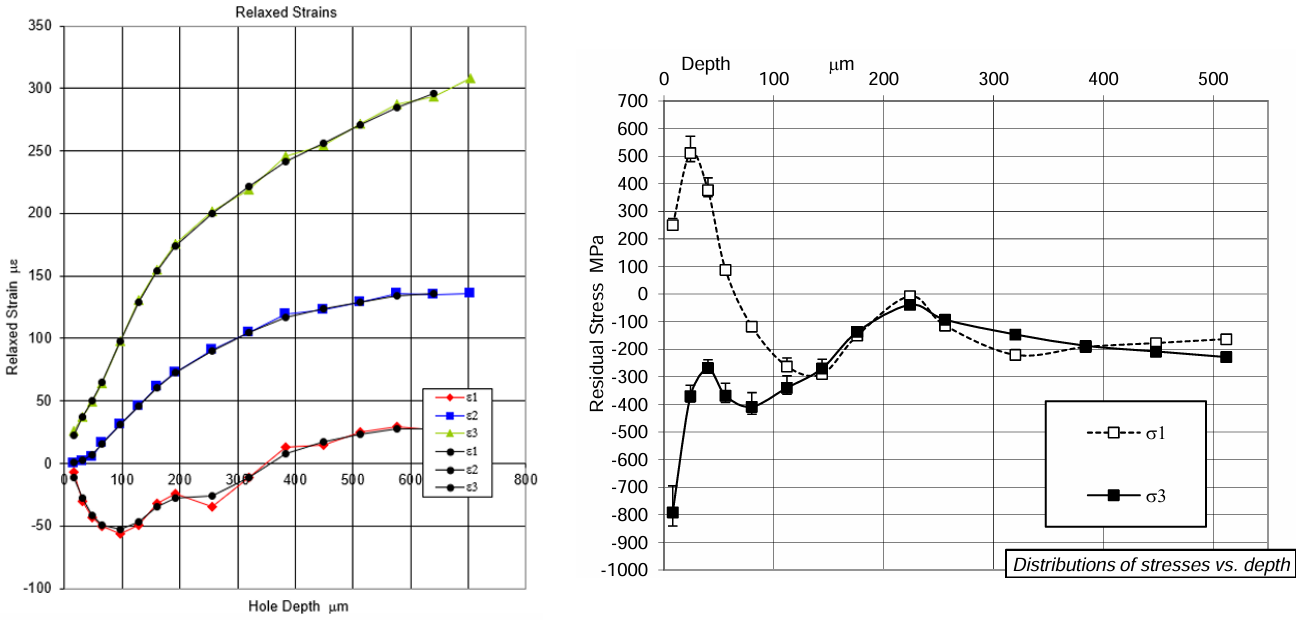

Figure 37. Recorded Microstrain Measurements (a) and Calculated Stresses (b) for Samples 3

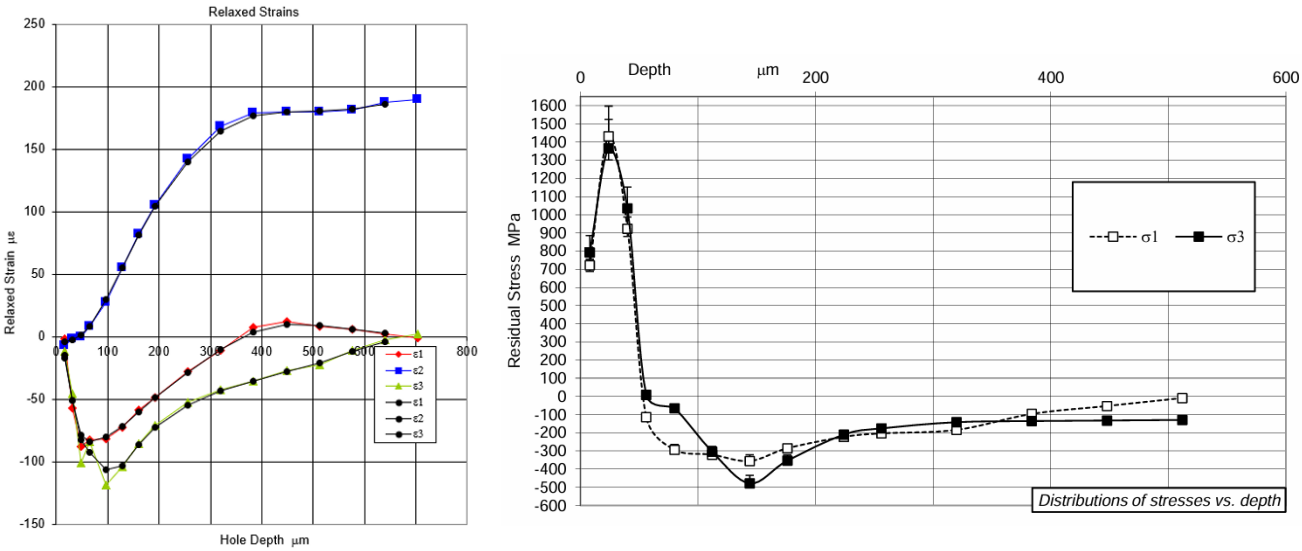

Figure 38 . Recorded Microstrain Measurements (a) and Calculated Stresses (b) for Samples 4

4.2.1. Data Analysis and discussion of Hole Drilling Measurement

The experimental design described in section 3.3.2, aimed for the evaluation of both the influences of clamping configuration and the number of deposited layers on residual stress built up, is used. The effects of varying the number of deposited layers on the resulting residual stress were evaluated based on the measured samples with the same clamping configuration. For samples with a constant number of layers, the influence of different clamping methods was compared. The choice of these specific clamping configurations is motivated by the need to understand how mechanical restraints applied during deposition may affect the distribution and magnitude of residual stresses. This investigation simulates the practical application case where during the manufacturing processes it involves temporary clamps with fixtures and their removal. Understanding the difference in residual stress levels with and without clamping helps informed decisions about clamping design and the long-term structural integrity of the deposited layers. Additionally, by evaluating the effect of different clamping configurations on samples with one and two deposition layers, which can help optimize deposition processes for different materials and applications.

In all samples, the most extreme stress values were observed near or just below 100 μm within the measured range, the observation from figures 35, 36, 37 and 38 are summarized as following.

- **Sample 1:** Both σ_1 and σ_3 displayed a similar trend. σ_1 started at approximately 250 MPa near the surface, dropped to -425 MPa by a depth of around 150 μm, and then steadily increased, crossing the 0 MPa mark around 400 μm. For σ_3, stresses began near 0 MPa, dropped to about -550 MPa at a depth of 80 μm, and gradually approached 0 MPa by the final measurement around 500 μm.

- **Sample 2:** σ_1 started at approximately 150 MPa at the surface, dropped to -100 MPa by around 100 μm, and then remained stable before gradually increasing after 300 μm, reaching near 0 MPa at 500 μm. For σ_3, stresses began close to 50 MPa, dropped to around -350 MPa by 100 μm, and then increased to approximately -100 MPa near 200 μm, remaining relatively constant level.

- **Sample 3:** The results for this sample showed a pattern of peaks and troughs. σ_1 began around 400 MPa near the surface, dropped to -250 MPa by 100 µm, rose to 0 MPa at 200 µm, and then gradually decreased again to -200 MPa at greater depths. For σ_3, stresses started close to -800 MPa, rose immediately to around -350 MPa, held steady until about 120 µm, and then increased to near 0 MPa at 200 µm before gently reducing to -200 MPa at the deepest increments.

- **Sample 4:** Both σ_1 and σ_3 showed very similar behavior. Both began around 750 MPa, peaked at approximately 1400 MPa, and dropped to near 0 MPa by around 50 µm. After this, a more gradual reduction occurred, reaching around -400 MPa by 150 µm, and then gently rising to around -100 MPa at the final measured depths. The first three data points in this sample were noticeably higher than those in the other samples, suggesting that surface finish effects may have contributed to the elevated values.

Based on these observations, the following discussions were made for helping the stress build up under different simulated situations of the clamping and when deposition with different number of layers.

a) Comparison of Sample 1 and Sample 2

Sample 1 and sample 2 were clamped along the centre of the base plate during deposition, while maintaining other deposition conditions consistent, the resulted residual stress within samples were mainly attributed from the number of the layer deposited. The residual stresses within Sample 1 have a more pronounced and sharper decline to highly negative stress levels near the surface. In contrast, sample 2 shows a more moderate decrease, with less fluctuation as depth increases. Due to the measurement depth limitation due to the type of the gauge rosette and drill used, only the top layer of the resulted residual stress can be measured. The observed results show that during the second layer of deposition, it can reduce the level of residual stress build up within the Stellite 6 layer deposited. This may be attributed to that i) during second layer deposition, there was remelting of the first layer; ii) second layer was deposited right after the first layer's deposition, effectively deposited on the preheated substrate. Both effects can largely reduce the residual stress build up within the second layer during its solidification process. In addition, as shown in table 7 the deflection of sample 2 remains similar to sample 1. This shows that plastic deformation occurred, that helped to further relax residual stress build up. The plastic deformation was expected during the second layer deposition which was constrained by the clamping. Hence the σ_1 along the deposition direction can be significantly reduced. As there were no clamping in the direction perpendicular to the deposition direction, all the residual stress builds up in this direction remain within the material, the measured σ_3 therefore shows the same trend for both samples 1 and 2 shown in figures 35 and 36, while within the sample 2, it has a relative lower residual stress build up due to the preheating that was induced during the first layer deposition. A similar effect was reported by Thawari et al. [21]. During the deposition of the second layer, significantly higher temperatures are observed at both surfaces of the material due to heat addition and conduction from the previously deposited layer. This sequential process leads to substrate preheating, which in turn reduces the thermal gradient across the material. The reduced thermal gradient is important in smoothing the transition in residual stress between the tensile and compressive regions, as observed in sample 2. Additionally, findings show that preheating has the greatest impact on reducing residual stress, as it minimizes the thermal gradient and subsequently the residual stress fluctuations during deposition [19].

b) Comparison of Sample 3 and Sample 4

Sample 3 shows a sharp drop-off from high initial stress levels near the surface, with fluctuating residual stresses across the depth as shown in figure 37-b. Sample 4, in contrast, exhibits much higher initial stress values (up to 1400 MPa), with a more stable and gradual reduction in stress over depth as shown in figure 38-b. This suggests that adding a second layer increases initial residual stress, but it also reduces sharp stress fluctuations at different depths, indicating a more uniform stress distribution in the 2-layers deposit as explained in previous section a), the reduced thermal gradient is important in smoothing the transition in residual stress of sample 4 [19,21].

Both sample 3 and sample 4 were clamped only on one side of the base plate, which deformations, induced by the thermal load during deposition, was shown in table 7. As the thermal expansion coefficient of SS316L at elevated temperature (20-1000 ºC, mean is 19.8×10^{-6}/ ºC) is larger than that of the Stellite 6 (20-1000 ºC, mean is 13.2×10^{-6} / ºC, the Stellite 6 is under tension during the solidification process [3]. The top surface of the deposited layer is where most of the thermal-induced strain is expected to remain, as this region experiences the highest thermal gradients, typically induced by the arc center. The arc center, with its high current density, provides the primary heat input during the deposition process. Thus, this is the location where found the peak residual stress is found as shown in figures 37 and 38. As there were no clamps to provide constraints for plastic deformation that can help residual stress relaxation, high level of residual stress within the deposited Stellite 6 layer were observed.

c) Comparison of Sample 1 and Sample 3

In the case of Sample 1, the clamping configuration firmly secured the base plate on both ends, ensuring a uniform constraint across the entire sample. This double-sided clamping minimized movement during the process, especially during cooling. The rigid clamping severely restricted thermal expansion, resulting in greater internal stresses during cooling. Therefore, the gradient of stress changes from tensile to compressive is very high and exhibited more significant stress variations, as shown in figure 35-b. This effect can be linked to the influence of thermal mismatch between the substrate and the cladding material, as noted in the literature [19]. Due to constrained thermal expansion, the material experiences higher levels of compressive thermal stress during the cooling phase, which then contributes to the observed residual stresses. However, the clamp provided constraint reduces the amount of strain accumulation along the deposition direction which reduce the level of the residual stress.

In contrast, Sample 3 employed a single-sided clamping configuration, which allowed for greater movement during the deposition and cooling process. As shown in figure 37-b, this more flat stress profile along the depth, can be attributed to the sample's ability to expand and contract more freely during the deposition process. This reduces the accumulation of residual stresses compared to the more constrained Sample 1. The reduced clamping constraint allows for material thermal expansion and contraction easier during thermal cycles where unconstrained materials tend to have a smoother thermal stress transition, leading to lower overall residual stresses. This aligns with the principle that lower thermal gradients result in more balanced stress distributions across the material [22].

d) Comparison of Sample 2 and Sample 4

In Samples 2 and 4 two layers are deposited, in clamped and unclamped conditions respectively. Sample 2, which utilized two clamps, exhibited moderate stress fluctuations with a stable stress profile as depth increased as shown in figure 36-b. In contrast, Sample 4, which used only one clamp, showed significantly higher residual stress peaks near the surface and greater variability in stress distribution below 50 µm compared to Sample 2 as shown in figure 38-b. The reason has been explained earlier when comparing sample 3 and 4. Overall, samples with a single clamp exhibited smoother stress distributions across greater depths. At larger depths, the increased freedom of movement provided by the single clamp resulted in reduced stress fluctuations.

4.2.2. Effect of Number of Layers and Clamping Method on Residual Stress

The measured residual stress reveals that the double-layered deposition can help managing the residual stress. Samples with two layers exhibit a more gradual reduction in residual stress with fewer sharp transitions between tensile and compressive regions. This is attributed to that during second layer's deposition, it not only partially remelts the first layer that reduce residual stress, but also can preheat the material reducing the thermal gradient and smoothing out stress variations. As a result, double-layer deposits provide a more balanced and stable residual stress profile, minimizing the risk of localized stress concentrations that can lead to material failure. When comparing clamping configurations, the single-sided clamping method shows a more smooth residual stress within the material than double-sided clamping. Single-sided clamping allows more freedom in thermal expansion and contraction during the deposition process, resulting in a smoother stress distribution and fewer fluctuations as depth increases. However, it has a drawback of large deformation and localized high residual stress build up.

By understanding these observation and measurements, the idea of pre-tension of the part or uniform clamping around the part to be deposited using Stellite 6 can be designed and implemented for the actual application case. Depending on the desired Stellite 6 thickness, multi-layer deposition strategy can be implemented to minimising the residual stress build up.

5. *Conclusions and Future Work*

This thesis has investigated the deposition of Stellite 6 on SS316L Stainless steel substrates using the GMAW-based WAAM process, with a focus on understanding the development and management of residual stresses. The research presents a foundation for improving the hardfacing process for future development of the automated toolpath generation. The main contributions of this thesis lie in its two key stages of investigation, as follows:

1. **First stage:** identified and transferred the optimal parameters for low heat input deposition of Stellite 6 on SS316L stainless steel substrate using a Miller GMAW welding system, despite its lack of the CMT capability. This stage included the following achievements:

- Achieved significant heat input reduction while maintaining deposition layer integrity and sufficient hardness.
- No defects or cracking in the Stellite 6 layer, addressing its inherent susceptibility to cracking during GMAW.
- Optimized parameters were tested and implemented in the production line, offering a more reliable and efficient WAAM process for industrial partners.

2. **Second stage:** by analysing residual stress distribution in GMAW-based WAAM Stellite 6 depositions using the hole drilling method, the better understanding of the residual stress build up will help for better clamping design and define deposition procedure for further development of the automated toolpath generation for deposition the Stellite 6 using WAAM. The following can be concluded from this study:

- The residual stress build up was comparable with other hardfacing methods, such as laser cladding [3], which make the hardfacing using WAAM becomes an economical viable process.
- GMAW-based WAAM can produce good hardfacing with lower residual stresses, suggesting it is a reliable technique to be adapted into industrial applications.
- Evaluated different clamping strategies, offering industrial partners insights into residual stress management and further automatic toolpath generation.
- The obtained results can serve a good foundation for integrating 3D vision monitoring and control systems for automated toolpath generation, progressing toward fully automated hardfacing or repair using WAAM.

Above all, this thesis not only help for a better understanding residual stress build up during Stellite 6 hardfacing using WAAM, but also offers practical solutions that can improve the efficiency and reliability of WAAM application in industrial settings. By providing a pathway towards more automated and controlled deposition processes, this research contributes to the broader goal of advancing WAAM technology for hardfacing and repair applications.

Based on the obtained results, it is recommended for carrying out the following task that will help to improve for better system development:

- It is recommended to implement the balancing residual stress management with dimensional stability for developing the reliable and automated repair or hardfacing solution, which includes adjusting the uniform clamping configuration, incorporating intermediate cooling steps or pretension to control deformation.
- It is recommended that future work involving advanced thermal modelling techniques to better simulate the heat distribution and their effects on residual stress for optimal toolpath to be generated automatically.
- It is recommended to combine multiple scale residual stress measurement techniques for a more comprehensive understanding of stress development at different scale.

References

[1] S. Bose, N. Sarkar, S. Vahabzadeh and D. Ke, "Additive Manufacturing of Ceramics," in Additive Manufacturing, Second Edition, CRC Press, 2019, pp. 183-231.

[2] S. Negi, S. Dhiman and R. k. Sharma, "Basics, applications and future of additive manufacturing technologies: A review," Journal of Manufacturing Technology Research, vol. 5, no. 1943-8095, 2013.

[3] W. Ya, "Laser materials interactions during cladding: analyses on clad formation, thermal cycles, residual stress and defects," University of Twente, 2015.

[4] A. Bandyopadhyay, Y. Zhang and S. Bose, "Recent developments in metal additive manufacturing," Current opinion in chemical engineering, vol. 28, no. 2211-3398, pp. 96-104, 2020.

[5] T. A. Rodrigues, V. Duarte, R. M. Miranda, T. G. Santos and J. P. Oliveira, "Current Status and Perspectives on Wire and Arc Additive Manufacturing (WAAM)," Materials, vol. 12, no. 1121, pp. 1-41, 2019.

[6] ASTM International, "ASTM F2792-12a: Standard terminology for additive manufacturing," ASTM International, West Conshohocken, PA, USA, 2012.

[7] N. Pellerin, S. Zielińska, S. Pellerin, F. Valensi, K. Musioł, C. d. Izarra, F. Briand and F. Richard, "Experimental investigations of the arc MIG - MAG welding," American Institute of Physics, vol. 812, no. 1, pp. 80-87, 2006.

[8] Z. Li, Y. Cui, J. Wang, C. Liu, J. Wang, T. Xu, T. Lu, H. Zhang, J. Lu, S. Ma, H. Fan and S. Tang, "Characterization of Microstructure and Mechanical Properties of Stellite 6 Part Fabricated by Wire Arc Additive Manufacturing," Metals, vol. 9, no. 4, 2019.

[9] M. Toozandehjani, F. Ostovan and M. Shamshirsaz, "Twin hot-wire arc welding additive manufacturing deposition of high tungsten Stellite-6 hard-facing coating: Processing, microstructure and wear properties," Materials Today Communications, vol. 35, no. 105572, 2023.

[10] Z. Lin, "Wire and arc additive manufacturing of thin structures using metal-cored wire consumables: microstructure, mechanical properties, and experiment-based thermal model," Mechanical Engineering Faculty of TUDelft, 2019.

[11] V. P. Group and Micro-Measurements, "Measurement of residual stresses by the hole-drilling* strain gage method," Tech Note TN-503, Revision: 01-Nov-2010.

[12] P. Withers and H. Bhadeshia, "Residual stress. Part 1 – Measurement techniques," Materials Science and Technology, vol. 17, no. 4, pp. 355-365, 2001.

[13] P. Withers and H. Bhadeshia, "Residual stress. Part 2 – Nature and origins.," Materials Science and Technology, vol. 17, no. 4, pp. 366-375, 2001.

[14] M. Roth, R. Hauert, A. Frenk, M. Pierantoni and E, Blank, "Residual stress formation in laser treated surfaces," Laser/Optoelektronik in der Technik/Laser/Optoelectronics in Engineering, St pp. 532-537, 1990.

[15] E. Bendek, I. Lira, M. Francois and C. Vial, "Uncertainty of residual stresses measurement by layer removal," International Journal of Mechanical Sciences, vol. 48, no. 12, pp. 1429-1438, 2006.

[16] G. P. Rajeev, M. Kamaraj and R. B. Srinivasa, "Comparison of microstructure, dilution and wear behavior of Stellite 21 hardfacing on H13 steel using cold metal transfer and plasma transferred arc welding processes," Surface & Coatings Technology, vol. 375, pp. 383-394, 2019

[17] F. da Silva, E. Braga, V. Ferraresi and F. Filho, "Coating weld cavitation erosion resistance using austenitic stainless steel and cobalt alloys deposited by GMAW and CW-GMAW," The Brazilian Society of Mechanical Sciences and Engineering, vol. 44, no. 569, 2022

[18] J. Murugan, S. Duraisamy, V. Priya and R. Arulmani, "Production and Evaluation of Microstructure and Mechanical Properties of Stellite 6 Prototype Parts by Robotic Wire Arc Additive Manufacturing,' Transactions of the Indian Institute of Metals, vol. 76, pp. 175-185 2023.
[19] Z. Lin, W. Ya, V. Subramanian, C. Goulas, B. di Castri, M. Hermans and B. Pathiraj, "Deposition of Stellite 6 alloy on steel substrates using wire and arc additive manufacturing," /nternationa/ journal of advanced manufacturing technology, vol. 111, no. 1-2, pp. 411-426, 2020.
[20] RAMLAB, "MAXQ Repair," RAMLAB. [Online]. Available: https://www.ramlab.com/maxq-repair/. [Accessed: 24-Oct-2023]
[21] Z. Li, Y. Cui, J. Wang, C. Liu, J. Wang, T. Xu, T. Lu, H. Zhang, J. Lu, S. Ma, H. Fan and S. Tang, "Characterization of Microstructure and Mechanical Properties of Stellite 6 Part Fabricated by Wire Arc Additive Manufacturing," Metals, vol. 9, no. 474, 2019.
[22] A. Gholipour, M. Shamanian and F. Ashrafizadeh, "Microstructure and wear behavior of stellite 6 cladding on 17-4 PH stainless steel," Journal of Alloys and Compounds, vol. 509, no. 14, pp. 4905-4909, 2011.
[23] M. K. Khouzani, A. Bahrami and M. YazdanMehr, "Spark plasma sintering of Stellite®-6 superalloy," Journal of Alloys and Compounds, vol. 782, pp. 461-468, 2019.
[24] A. E. Pilehrood, A. Mashhuriazar, A. H. Baghdadi, Z. Sajuri and H. Omidvar, "ffect of Laser Metal Deposition Parameters on the Characteristics of Stellite 6 Deposited Layers on Precipitation-Hardened Stainless Steel," Materials, vol. 14, no. 5662, 2021.
[25] N. Thawari, C. Gullipalli, A. Chandak and T. V. K. Gupta, "Influence of laser cladding parameters on distortion, thermal history and melt pool behaviour in multi-layer deposition of stellite 6: In-situ measurement," Journal of Alloys and Compounds, vol. 860, no. 157894, 2021.
[26] Y. Guo, Z. Wang, Y. Liu, J. Xiong, J. Zhang and H. Zhang, "Study on Residual Stress Distribution in Stellite−6 Cladding Layers on 420 Steel Steam Turbine Blades," Journal of Materials Engineering and Performance, pp. 1-12, 2023.
[27] R. H. Leggatt, "Residual stresses in welded structures," International Journal of Pressure Vessels and Piping, vol. 85, no. 3, pp. 144-151, 2008.
[28] Y. Liu,J. Shi and Y. Wang, "Evolution, Control, and Mitigation of Residual Stresses in Additively Manufactured Metallic Materials: A Review," Advanced Engineering Materials, vol. 25, no. 22, 2023.
[29] B. Ahmad, x. Zhang, H. Guo, M. E. Fitzpatrick, L.M.S.C.Neto and S. Williams, "Influence of deposition strategies on residual stress in wire+ arc additive manufactured titanium Ti-6Al- 4V," Metals, vol. 253 no. 12(2), 2022.
[30] S Ghosh and J, Choi., Modeling and experimental verification of transient/residual stresses and microstructure formation in multi-layer laser aided DMD process, vol. 128, no. 7, pp. 662-679, 2006.
[31] T. Amine,J. W. Newkirk and F. Liou, "Investigation of effect of process parameters on multilayer builds by direct metal deposition," Applied Thermal Engineering, vol. 73, no. 1, pp. 500-511, 2014.
[32] L. Sun, X. Ren, J. He and Z. Zhang, "Numerical investigation of a novel pattern for reducing residual stress in metal additive manufacturing," Journal of Materials Science & Technology, vol. 67, pp. 11-22, 2021
[33] M. A. Somashekara, M. Naveenkumar, A. Kumar, C. Viswanath and S. Simhambhatla "Investigations into effect of weld-deposition pattern on residual stress evolution for metallic additive manufacturing.," International Journal of Advanced Manufacturing Technology, vol. 90, pp. 2009-2025, 2017.
[34] T. N. TN, "Measurement of residual stresses by the hole-drilling* strain gage method," 1993.

[35] F. Faure and R. H. Leggatt, "Residual stresses in austenitic stainless steel primary coolant pipes and welds of pressurized water reactors," International journal of pressure vessels and piping, vol. 65, no. 3, pp. 265-275, 1996.
[36] M.S.S. Yi and J.S. Park, "Study of heat source model and residual stress caused by welding in GMAW of Al alloy," Metals, vol. 12, no. 6, 2022.
[37] G. Farrahi, G. H. Majzoobi and A. Fadaee, "Prediction by genetic algorithm and measurement by center hole drilling of residual stresses of MAG weldment," Advanced Materials Research, vol. 83, pp. 738-745, 2010.
[38] P. K. Ghosh and A. K. Ghosh," Control of residual stresses affecting fatigue life of pulsed current gas-metal-arc weld of high-strength aluminum alloy," Metallurgical and Materials Transactions, vol. 35, pp. 2439-2444, 2004.
[39] Auto-Continuum™ Systems, Automated MIG Welding Systems, Issued Mar. 2022, Index No. AU/10.0.
[40] Miller Owner's Manual, Millermatic 350P Aluminum, Issued 2013, OM-254 915C
[41]SkyCiv Engineering, [Online]. Available: https://skyciv.com/docs/tutorials/stress-tutorials/calculate-bending-stress-of-a-beam-section/. [Accessed 30 9 2024].
[42] Strain Indicator and Recorder, Micro-Measurements, 2011.
[43] Leif Kayser, Eleif.net. [Online]. Available: https://eleif.net/. [Accessed: Oct. 15, 2023].
[44] G. S, Schajer, "Measurement of Non-Uniform Residual Stresses Using the Hole-Drilling Method. Part ll--Practical Application of the Integral Method," Engineering materials and technology, vol. 110, no. 4, pp. 344-349, 1988.
[45] J. Everaerts, E. Salvati, and A. M. Korsunsky, "Nanoscale Depth Profiling of Residual Stresses Due to Fine Surface Finishing," *Adv. Mater. Interfaces*, vol. 6, no. 19, 1900947, 2019.
[46] N. Mäkipää, "Surface characterization of ground surfaces: effects of grinding," Master's thesis, 2019.

Appendices

Appendix A

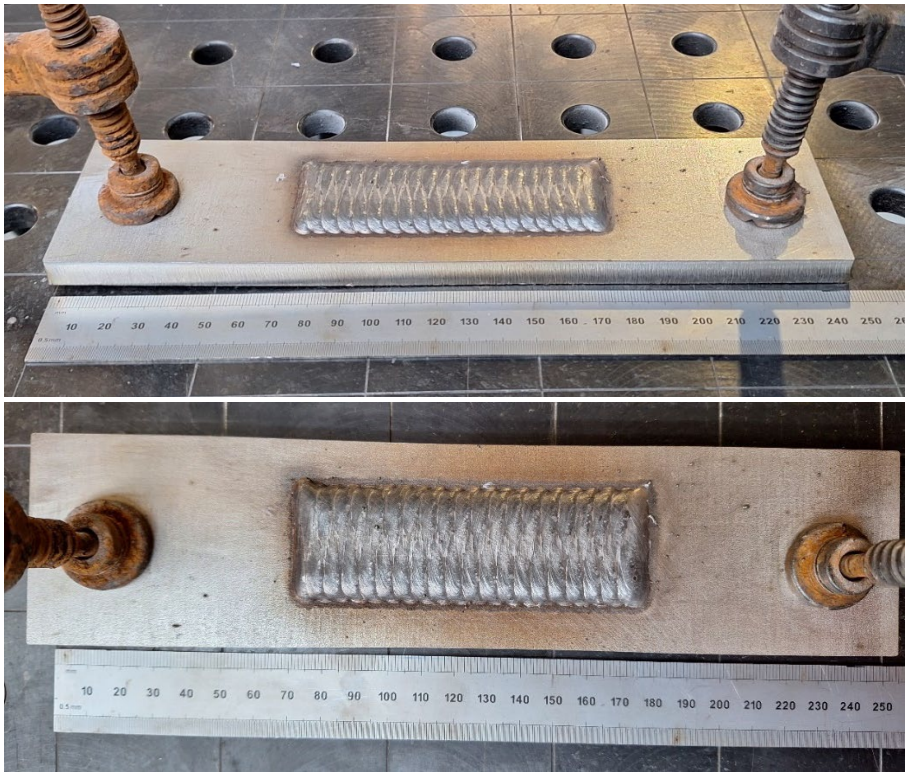

Figure 39. Side (a) and Top (b) views of sample 1 before unclamping

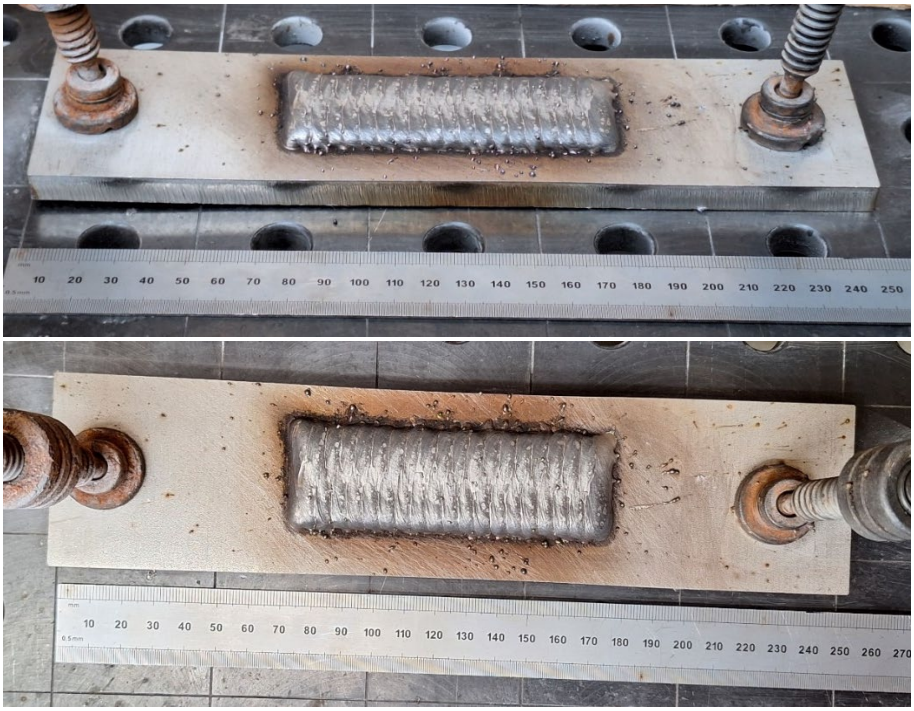

Figure 40. Side (a) and Top (b) views of sample 2 before unclamping

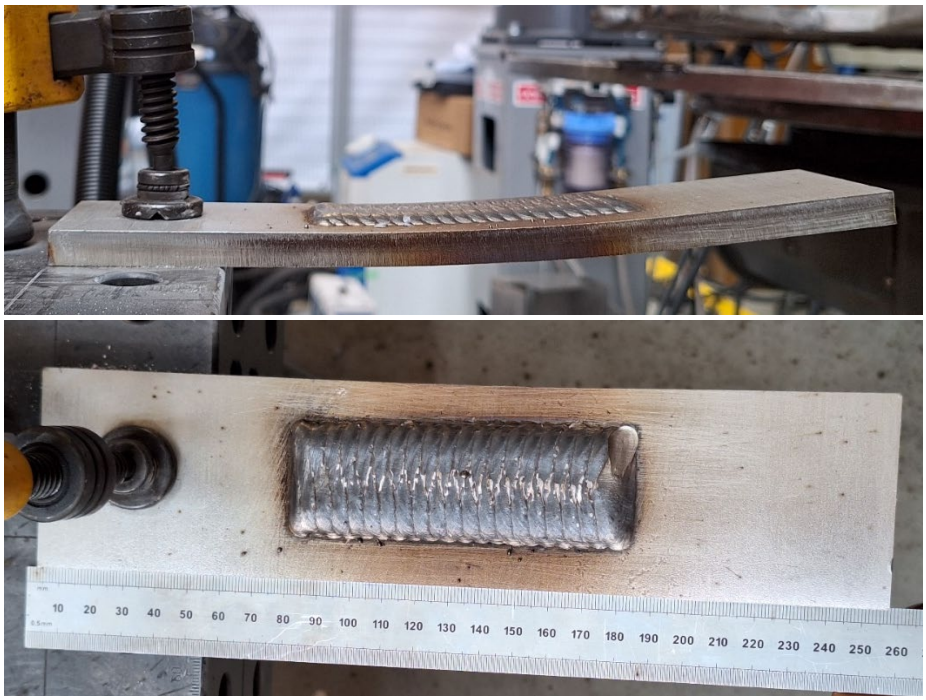

Figure 41. Side (a) and Top (b) views of sample 3 before unclamping

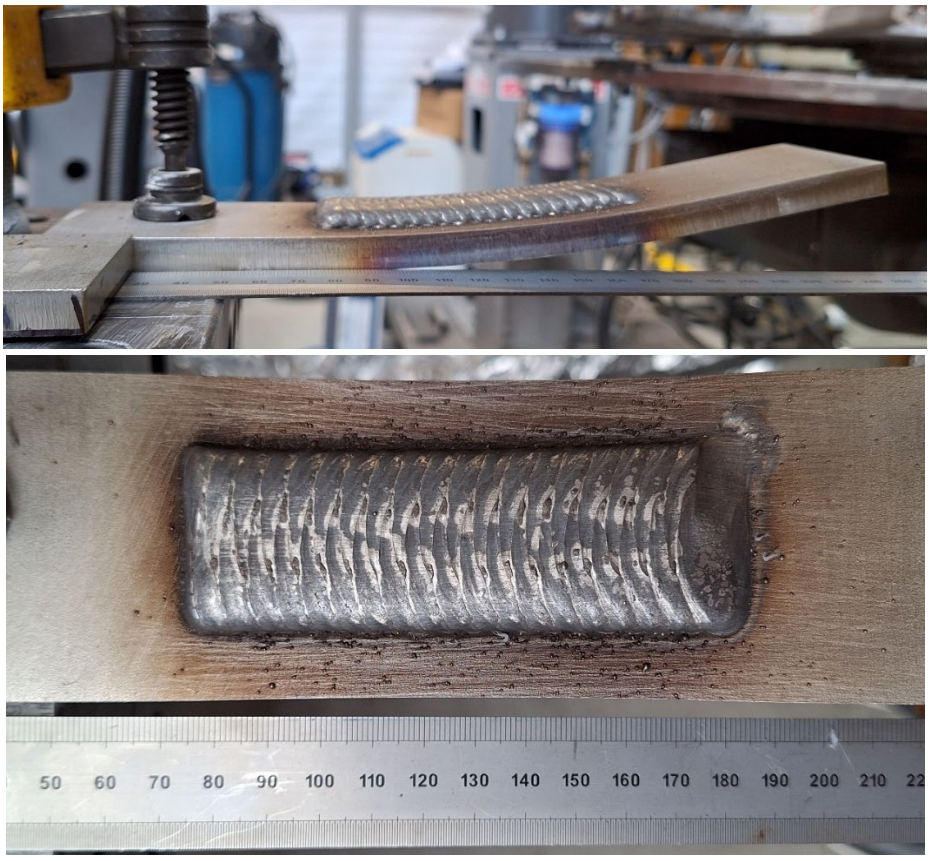

Figure 42. Side (a) and Top (b) views of sample 4 before unclamping

Appendix B

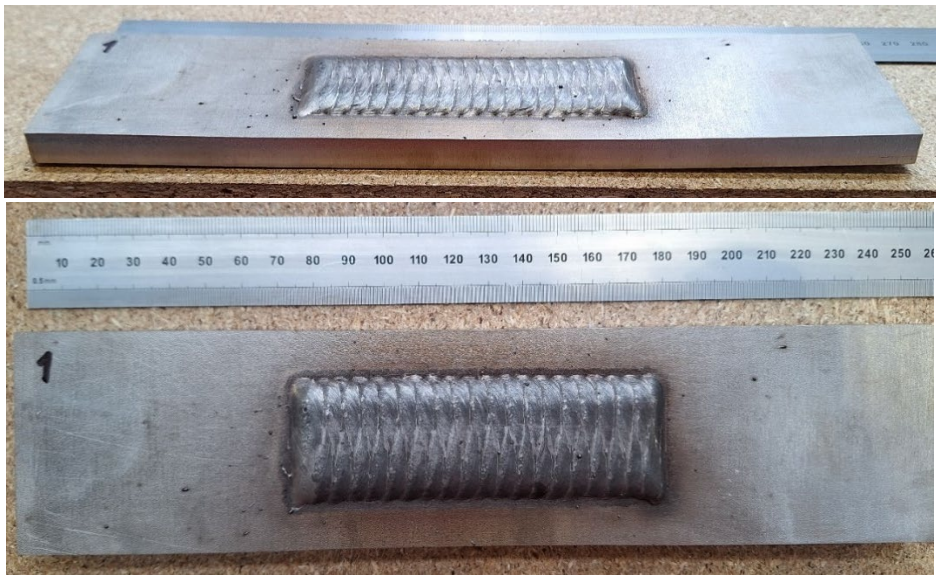

Figure 43. Side (a) and Top (b) views of sample 1 after unclamping

Figure 44. Side (a) and Top (b) views of sample 2 after unclamping

Figure 45. Side (a) and Top (b) views of sample 3 after unclamping

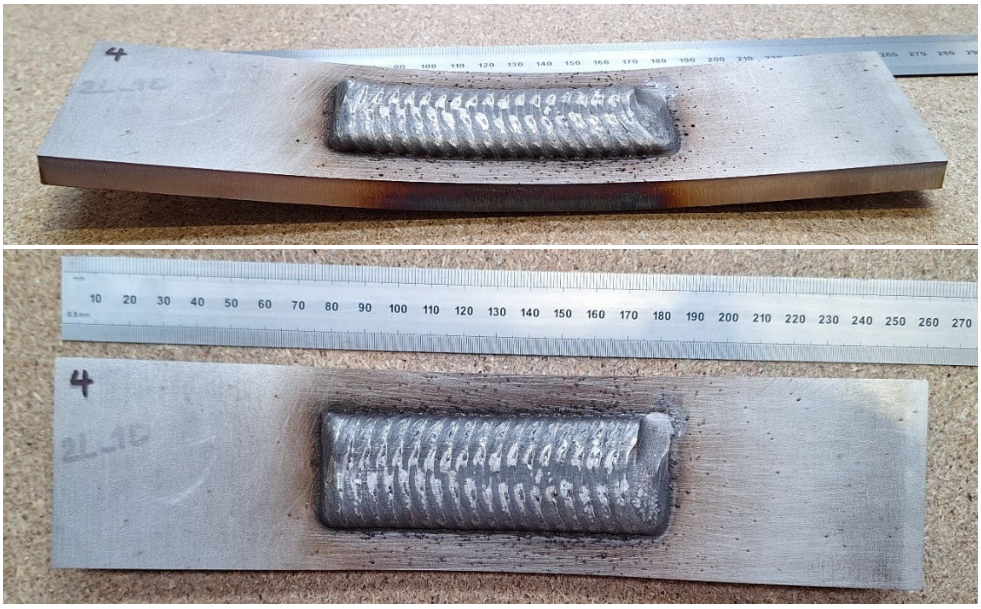

Figure 46. Side (a) and Top (b) views of sample 4 after unclamping

Figure 47. Comparative Top (a) and Side (b) views of all samples after unclamping